PHYSICAL REVIEW B **91**, 134202 (2015)

First-principles study of a sodium borosilicate glass-former. II. The glass state

Laurent Pedesseau
Laboratoire Charles Coulomb, UMR 5221, Université Montpellier and CNRS, 34095 Montpellier, France
and Université Européenne de Bretagne, INSA, FOTON, UMR 6082, 35708 Rennes, France

Simona Ispas[*] and Walter Kob[†]
Laboratoire Charles Coulomb, UMR 5221, Université Montpellier and CNRS, 34095 Montpellier, France

(Received 20 July 2014; revised manuscript received 3 February 2015; published 6 April 2015)

We use *ab initio* simulations to investigate the properties of a sodium borosilicate glass of composition $3Na_2O$-B_2O_3-$6SiO_2$. We find that the broadening of the first peak in the radial distribution functions $g_{\mathrm{BO}}(r)$ and $g_{\mathrm{BNa}}(r)$ is due to the presence of trigonal and tetrahedral boron units as well as to nonbridging oxygen atoms connected to BO_3 units. In agreement with experimental results, we find that the $^{[3]}$B units involve a significant number of nonbridging oxygens, whereas the vast majority of $^{[4]}$B have only bridging oxygens. We determine the three-dimensional distribution of the Na atoms around the $^{[3]}$B and $^{[4]}$B units and use this information to explain why the sodium atoms associated with the latter share more oxygen atoms with the central boron atoms than the former units. From the distribution of the electrons we calculate the total electronic density of states, as well its decomposition into angular momentum contributions. The vibrational density of states shows at high frequencies a band that originates from the motion of the boron atoms. We find that the $^{[3]}$B and $^{[4]}$B units give rise to well-defined features in the spectrum, which thus can be used to estimate the concentration of these structural entities. The contribution of $^{[3]}$B can be decomposed further into symmetric and asymmetric parts that can also be easily identified in the spectrum. Furthermore, it is found that certain features in the spectrum can be used to obtain information on the type of atom that is the second-nearest neighbor of a boron in the $^{[4]}$B unit. We calculate the average Born charges on the bridging and nonbridging oxygen atoms and show that these depend linearly on the angle between the two bonds and the distance from the connected cation, respectively. Finally, we have determined the frequency dependence of the dielectric function, as well as the absorption spectra. The latter is in good quantitative agreement with the experimental data.

DOI: 10.1103/PhysRevB.91.134202 PACS number(s): 61.43.Fs, 63.50.Lm, 71.15.Pd

I. INTRODUCTION

Sodium borosilicate (NBS) glasses are an important class of materials since they are resistant to thermal shocks, chemically inert, mechanically strong, and have good insulating properties. As a consequence one finds them in a multitude of applications such as glassware in the laboratory, utensils in the kitchen, or in glass wool for insulation. Many of these properties are related to the way the cations Si and B build up the network of the glass. However, since boron can form three- and fourfold coordinated structural units (i.e., triangles, $^{[3]}$B, or tetrahedra, $^{[4]}$B) which have rather different mechanical and electronic behavior, our knowledge on the global structure of the network is far from complete [1].

Using solid-state nuclear magnetic resonance (NMR) spectroscopy of ^{11}B, Yun, Bray, Dell, and co-workers have investigated intensively the structural properties of NBS glasses [2–4]. Based on these experiments, they have proposed a structural model (called hereafter YBD) which describes the evolution of the structure and the mechanism of creation of nonbridging oxygens in terms of the two parameters $K = [SiO_2]/[B_2O_3]$ and $R = [Na_2O]/[B_2O_3]$, where [·]'s indicate mol%. The YBD model assumes that the borosilicate glasses contain several larger structural units like diborate, pyroborate, boroxol rings, reedmergnerite, and danburite, which are also referred to as suprastructural units [1]. These units are, in turn, composed of more basic units, such as four-coordinated silicon, three- and four-coordinated borons, etc. Within the model the Na_2O-B_2O_3-SiO_2 ternary diagram is divided into four compositional regions and for each domain the YBD model predicts the fraction of $^{[3]}$B and $^{[4]}$B, as well as the fraction of bridging oxygens. In particular, it is postulated that BO_3 units are transformed to BO_4 if $R \leqslant 0.5$, with sodium acting as charge compensator, while for $0.5 < R \leqslant R^*$ open reedmergneritelike structures are formed on intermediate length scales. (Here the threshold composition is given by $R^* = 0.5 + K/16$ and corresponds to compositions for which the additional cations start to form nonbridging oxygen connected to silica tetrahedra.) These latter structures consist of a BO_4 tetrahedron surrounded by four SiO_4 tetrahedra.

Subsequently, Raman spectroscopy has been used in an attempt to gain insight into the structure of NBS glasses [5–9]. For this, researchers assigned certain bands of the spectrum to medium range order structures, but so far no consensus has emerged on how this should be done. Based on certain features of Raman spectra measured for sodium borosilicate glasses at different temperatures, Manara *et al.* [8,9] recently proposed a revision of the YDB model. The peaks around 580 and 630 cm^{-1}, which are two of the main features in the 550–850 cm^{-1} frequency range, were assigned to breathing modes of borosilicate reedmergneritelike and danburitelike rings, respectively. (Reedmergneritelike ring includes one BO_4

---

[*] simona.ispas@univ-montp2.fr
[†] walter.kob@univ-montp2.fr

tetrahedron and three SiO_4 tetrahedra, while the danburitelike ring includes two BO_4 tetrahedra and two SiO_4 tetrahedra. See Ref. [8] for an illustration of the two superstructures.) In practice, this modification of the YBD model shifts the boundary composition R^* to $R^* = 0.5 + K/2N$, with a value of N between 5 and 6.

In a previous paper, subsequently referred to as Part I [10], we have studied the properties of an NBS system of composition $3Na_2O$-B_2O_3-$6SiO_2$ in the *liquid* state. In the present paper we investigate the properties of the corresponding *glass*. In particular, we focus on the structures around the boron atoms and how these are embedded into the network. In addition, we also discuss the electronic and vibrational properties of the system and how these are related to the structural units. These studies will make it possible to gain direct insight into the structural properties of the NBS glass considered and also help to interpret experimental data for glasses that have a similar composition.

The remaining of the paper is organized as follows. We start with a brief reminder of the simulation procedure and give the details on how the glass samples have been produced. In Sec. III we discuss the structural properties of the glass. Section IV is devoted to the vibrational properties of the system. This is followed by Sec. V in which we present the electronic properties of the sample, as well as the charges of the various species and how these are related to the local geometry. Section VI deals with the dielectric properties of the system and in Sec. VII we summarize and conclude the paper.

II. SIMULATION DETAILS

We have used the Vienna *ab initio* package (VASP) [11,12] to carry out first-principles molecular dynamics (MD) simulations. The system considered is $3Na_2O$-B_2O_3-$6SiO_2$ and the samples had 320 atoms (60 silicon, 180 oxygen, 60 sodium, and 20 boron atoms). The size of the cubic box was 15.97 Å, which corresponds to a mass density of 2.51 g/cm^3 (the experimental value of the density for NBS [13]), and periodic boundary conditions were used. The electronic structure calculations were carried out within the Kohn-Sham (KS) approach of the density functional theory (DFT) [14,15] using the generalized gradient approximation (GGA) and the PBEsol functional [16,17]. A plane-wave basis at the Γ point and the projector-augmented-wave (PAW) formalism [18] were used for the expansion of the KS orbitals and for the description of the electron-ion interaction, respectively. The choice of the functional as well as other simulations parameters has been detailed in Ref. [10].

The results discussed in this work for the glass at 300 K were averaged over six samples generated with different quench rates and annealing histories (more details are given in Ref. [10] and below). Despite their different thermal histories, we have not detected any significant dependence of the glass properties on the production process. These glass samples were generated using a two-stage quench protocol in order to save CPU time and taking into account that the glass structural properties do not change below the glass transition temperature, which, in our simulations, is around 2000 K due the high quench rates.

To generate the glass samples, we have equilibrated two independent liquid samples at 3000 K, i.e., in the liquid. We then started a linear quench first from 3000 K to 2000 K (using a quench rate of 2×10^{14} K s^{-1}) and then a quench from 2000 K to 300 K with a rate of 1.7×10^{15} K s^{-1}. In addition, we used four independent liquid configurations at 2200 K and started from them a quench to 1200 K with a rate of 2×10^{14} K s^{-1}, followed by a quench with rate 9×10^{14} K s^{-1} to 300 K. Four of these six glass samples were annealed for 2 ps keeping the temperature fixed at 300 K, and for two of them this annealing was followed by NVE runs of 8 and 15 ps, respectively.

For the electronic densities of states and vibrational properties, we quenched the samples to 0 K and relaxed them. This relaxation was stopped once the x, y, z components of the forces acting on each atom were less than 10^{-3} eV/Å. The data discussed in Secs. IV and VI were obtained by averaging over eight samples, since two additional samples have been generated by infinitely fast quenches (i.e., steepest descent) from the two liquid trajectories at 3700 K.

III. STRUCTURE

In this section we discuss the structural properties of the glass, notably the environment of three- and fourfold coordinated boron atoms, as well as the arrangement of the sodium atoms around the network-formers.

A. Radial pair distribution functions

The partial radial pair distribution function (PDF) $g_{\alpha\beta}(r)$ is proportional to the probability to find an atom of type α at a distance r from an atom of type β (see Eq. (1) in Part I [10]). The various PDFs have been shown in Figs. 1 and 2 of Part I at different temperatures for the liquid as well as for the glass state [10]. For the latter we have found that the PDFs for Si-O and B-O go to zero between the first- and second-nearest-neighbor peaks. Thus, this feature makes it possible to define in an unambiguous manner which oxygen atom is a first-nearest neighbor of a given Si or B atom and hence to determine the number of O atoms that are bonded

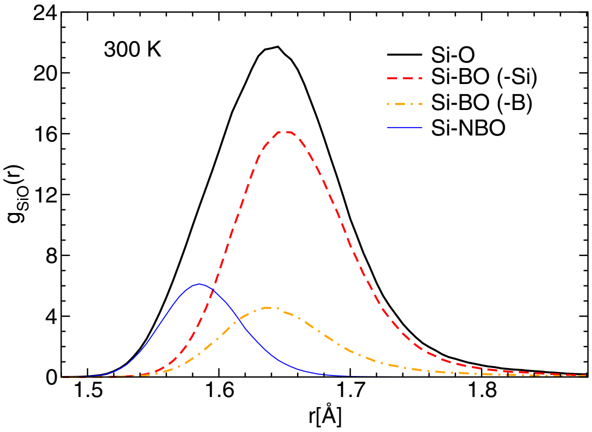

FIG. 1. (Color online) First peak of the Si-O PDF for the glass decomposed by taking into account the oxygen type (BO and NBO), as well as the nature of the type of the second neighbor of the O atom.

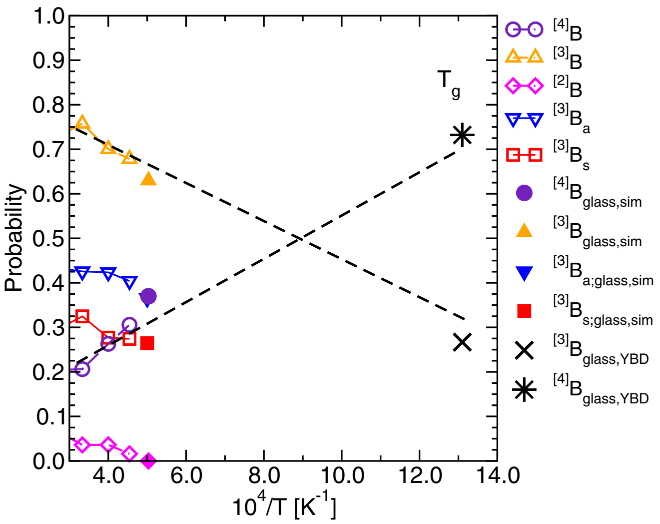

FIG. 2. (Color online) Temperature dependence in the liquid state of the concentrations of two-, three-, and fourfold coordinated borons as well as the ones of the symmetric and asymmetric threefold borons, $^{[3]}B_s$ and $^{[3]}B_a$ respectively. The solid symbols are the corresponding concentrations in the glass. The dashed lines are the extrapolation of the three- and fourfold coordinated borons to low temperatures, taking into account that they have to sum up to 100%. The star and cross are the corresponding concentrations as predicted by the YBD model (shown at $T = 763$ K, the experimental glass transition temperature).

TABLE I. Structural features of the NBS glass and of the liquid at 2200 K: Bond lengths, bond angles, concentration of $Q^{(n)}$ units, oxygen species (BO, NBO, tricluster oxygen), as well as boron coordinations. For the Bond lengths, the values correspond to the positions of the first peak of the corresponding PDFs plotted in Figs. 1 and 2 of Ref. [10]. For the bond angle we give in parentheses also the standard deviation of the distribution.

	Glass	Liquid at 2200 K
Si-O bond length (in Å)	1.64	1.63
Si-BO bond length	1.64	1.63
Si-NBO bond length	1.58	1.58
B-O bond length	1.42	1.38
B-BO bond length	1.42	1.40
B-NBO bond length	1.33	1.30
Na-O bond length	2.29	2.24
$\widehat{\text{SiOSi}}$ (°) bond angle	132.7 (15.0)	130.9 (18.1)
$^{[5]}$Si (%)	7.5	10.6
$Q^{(4)}$ (%)	35.3	33.6
$Q^{(3)}$ (%)	49.8	48.2
$Q^{(2)}$ (%)	6.8	7.0
$Q^{(1)}$ (%)	0.3	0.1
BO (%)	73.2	71.9
NBO (%)	26.7	27.3
TBO (%)	0.1	0.8
$^{[4]}$B (%)	37.0	30.5
$^{[3]}$B (%)	63.0	67.8

to the network-formers. From that information we then can identify the so-called $Q^{(n)}$ species, i.e., the Si atoms that have exactly four oxygen atoms as nearest neighbor, n of which are bonded to another network forming atom. In Table I we summarize the so-obtained information regarding the various length of the bonds, the fraction of $Q^{(n)}$ species, as well as the concentration of three- and fourfold coordinated boron atoms. The same quantities are also given for 2200 K, i.e., the liquid at the lowest temperature at which we have been able to equilibrate the system. As expected, the values of these quantities in the liquid are quite close to the ones in the glass state, since, due to the rapid quenching, the main difference in the structure is an anharmonic relaxation of the positions of the atoms.

From Fig. 1(a) of Part I (inset) one sees that the first-nearest-neighbor peak in $g_{\text{SiO}}(r)$ is rather sharp. However, a closer inspection shows that the peak is, in reality, a superposition of three distinct peaks that are at slightly different positions. This is demonstrated in Fig. 1, where we show this PDF decomposed into contributions according to the different oxygen species: bridging oxygen (BO) linking to either Si or B and nonbridging oxygen (NBO). We see that the Si-O-Si-peak is at a distance ($r_{\text{max}} \approx 1.65$ Å) that is only slightly larger than the one for Si-O-B ($r_{\text{max}} \approx 1.64$ Å), which shows that, in this case, the nature of the second-nearest neighbor does not influence the bond distance to the first-nearest neighbor. More important is the observation that the peak in Si-O-Si is significantly higher than the one for Si-O-B. If the network would be completely random, one would expect a factor of three (since we have 3 times more Si atoms than B atoms). However, we find that the ratio between the peak heights is significantly higher than 3; i.e., the mixing of the two networks is not ideal, in qualitative agreement with the observation in Part I, where we found that the Si and B atoms undergo a microphase separation [see the partial structure factor $S_{\text{SiB}}(q)$ shown in Fig. 6(b) of Part I]. Finally, we see that the distribution for the NBO shown in Fig. 1 indicates that this oxygen species is relatively close to the Si atom ($r_{\text{max}} \approx 1.58$ Å), a result that is reasonable in terms of charge balance and in good qualitative agreement with previous *ab initio* simulations for binary sodium and lithium silicate glasses [19–22], as well as more complex bioactive glasses [23]. We note that the splitting between Si-BO and Si-NBO bond lengths has not been observed in classical MD simulations for a different borosilicate composition [24], showing that effective potentials have difficulty in catching such subtle effects.

Regarding the PDF for B-O, we will see below that it is useful to decompose this correlation function into contributions that stem from the trigonal motifs $^{[3]}$B and the tetragonal ones, i.e., $^{[4]}$B, since these are important building blocks in the network. Before doing this it is, however, important to see to what extent the concentration of these motifs depends on the way we have produced the glass. Although the structure of all glasses will depend to some extent on the production history, this dependence is usually mild and, hence, can, to a first approximation, be neglected [25]. However, the case of borate systems is special since in the liquid state there is a significant conversion of threefold coordinated boron atoms into fourfold coordinated ones if temperature is decreased and hence it must be expected that the properties of the glass depend strongly on its fictive temperature. To estimate this dependence, we show in Fig. 2 the T dependence of the concentration of two-, three-, and fourfold coordinated boron atoms in the liquid (open symbols). As can be seen, the concentration of twofold coordinated boron atoms is small, decreases very rapidly, and vanishes at around 2000 K. Hence, we conclude that this local structure is not relevant in this type of glass, in agreement with expectation and experiments. Also the concentration of $^{[3]}$B decreases if T is lowered, but remains at relatively high values in the whole temperature range at which we can probe the equilibrium properties of the liquid. In contrast to this, the concentration of $^{[4]}$B is relatively small at high T, but increases steadily if temperature is lowered. The significant T dependence that we find for the concentration of $^{[3]}$B and $^{[4]}$B is in qualitative agreement with results from NMR experiments in various borosilicate glasses for which it has been found that an increase of the quench rate by 4–6 orders of magnitude leads to a decrease of the concentration of $^{[4]}$B by about 5%–7% [26–29] and that the concentration of $^{[3]}$B is increasing with increasing T [27,29–31]. In studies on samples at high temperatures it has been shown that an increase of annealing time of the glass leads to higher concentration of $^{[4]}$B [32].

In view of this quite strong T dependence of the concentrations of $^{[3]}$B and $^{[4]}$B, it is evident that a glass produced with the high quenching rates imposed by the *ab initio* simulations will not give a reliable prediction for these concentrations in a real glass. This is seen in Fig. 2, where we also show these concentrations for the glass we have obtained (solid symbols). As expected, these concentrations are very close to the values we have extracted for these quantities in the liquid at the lowest temperature, i.e., 63% and 37% for $^{[3]}$B and $^{[4]}$B, respectively. However, since we have determined the T dependence of these concentrations, we can extrapolate them to the temperature at which the *real* liquid undergoes a glass transition temperature and hence obtain a more reliable prediction for these values. This extrapolation, in which we have taken into account that the sum of the two concentrations must add up to 100%, is included in Fig. 2 as well (dashed lines). We see that for $T_g \approx 760$ K one obtains values that are close to the ones predicted by the YBD model (25% and 75% for $^{[3]}$B and $^{[4]}$B, respectively, show in the figure as well) and also to the ones estimated from x-ray absorption near-edge structure experiments (22% and 78%, respectively) [33]. The agreement between simulation and the prediction of the YBD model improves even further, if we assume that the concentration of the $^{[3]}$B and $^{[4]}$B shows a T dependence even a bit below T_g, an assumption that is certainly reasonable. Hence, we can conclude that our simulations do indeed make it possible to predict the mentioned concentrations in the real glass, *if one takes into account their T dependence*.

Having understood the T dependence of the concentrations of $^{[3]}$B and $^{[4]}$B, we return to the discussion of the PDF for B-O, and in Fig. 3 we show the first peak of this function. In view of the importance of the local motifs $^{[3]}$B and $^{[4]}$B, we have decomposed this peak into the contributions from trigonal and tetrahedral boron (full and dashed lines, respectively).

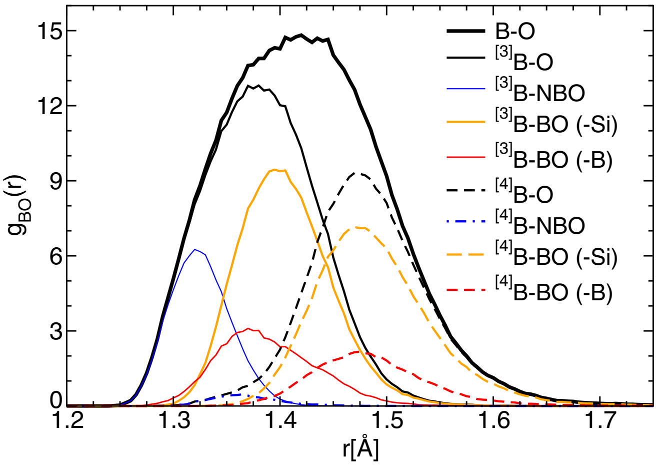

FIG. 3. (Color online) First peak of the B-O PDF for the glass, decomposed into contributions from $^{[3]}$B and $^{[4]}$B, into oxygen's speciation BO and NBO, as well as according the second network-former of the bridge B-O-T, for T = Si, B.

From the graph we see that the length of the B-O bond is 1.38 and 1.47 Å for $^{[3]}$B-O and $^{[4]}$B-O, respectively. These values are in excellent agreement with the ones obtained from neutron scattering experiments on B_2O_3 and binary borate glasses, which gave 1.37 and 1.47 Å, respectively [34], or on sodium diborate glass, which gave 1.38 Å for the $^{[3]}$B-O distance and 1.485 Å for the $^{[4]}$B-O distance [30]. Our values are also close to the ones obtained within a classical MD simulation of borosilicate glasses [24,35], thus showing that these distances do not depend strongly on the composition. It is therefore noteworthy that a reverse Monte Carlo simulation of borosilicate glasses with quite similar Na_2O/B_2O_3 and SiO_2/B_2O_3 ratios, but containing 5% BaO-5% Zr_2O, gave a $^{[4]}$B-O distance around 1.60 Å [36], which indicates that this approach does not give reliable results.

Although the position of the first peaks in $^{[3]}$B-O and $^{[4]}$B-O are very close to the ones found in pure B_2O_3 or binary borates, one has to realize that the local structure of the present system is more complex. In particular, the presence of Na makes that there is a significant concentration of NBO, with the consequence that the B-O distance shows a relatively wide distribution. This can be seen in Fig. 3, where we show also the decomposition of the $^{[3]}$B-O and $^{[4]}$B-O distributions into the parts involving BO and NBO atoms. From the size of the peaks, one sees immediately that the NBOs play only a minor role for the $^{[4]}$B environment (1.2%), whereas in the case of the $^{[3]}$B structures they account for 18% of the bonds. Hence, we conclude that NBOs are mainly associated with the trigonal motifs. A similar conclusion has been reached from classical MD simulations for a borosilicate glass with a different composition [24].

The location of the NBO peaks is shifted significantly to smaller distances with respect to the ones for the BO, a result that, in view of the reduced connectivity of the NBOs, is reasonable. For the $^{[3]}$B-NBO distribution we find the peak at 1.32 Å, whereas the one for $^{[3]}$B-BO is at 1.39 Å. That the *mean* position of the $^{[3]}$B-O peak is basically the same as the ones found for B_2O_3 (for which one does not expect to have NBO) is therefore only due to the effect of averaging the peaks for the $^{[3]}$B-NBO and $^{[3]}$B-BO.

Finally, we mention that the length of the B-O bond can also be influenced by the second atom that is connected to the oxygen: For the case of a $^{[3]}$B-O bond in which the O is

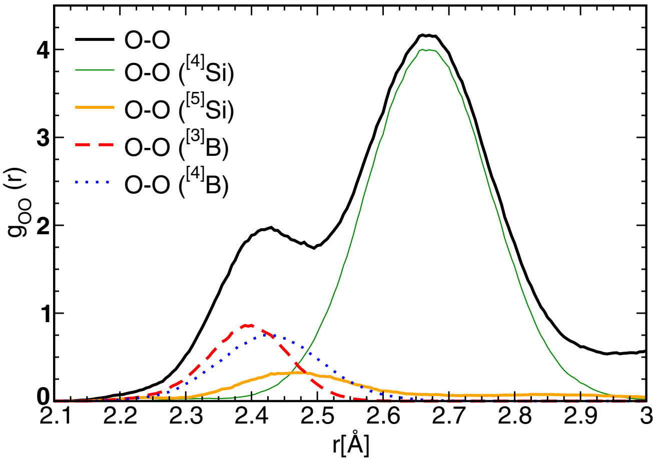

FIG. 4. (Color online) First peak of the O-O PDF decomposed into contributions of oxygen atoms that are associated with $^{[3]}$B, $^{[4]}$B, and four- and fivefold coordinated Si.

attached to a B or Si atom the bond length is 1.37 and 1.40 Å, respectively. However, for the case of a $^{[4]}$B-O bond we do not find such a difference, thus showing that the boron triangles and tetrahedra have quite different rigidity.

Figures 1 and 3 show that there is a substantial amount of NBOs in our system and we find that the total concentration is 27% (i.e., the BO have a concentration of 73%). Although we have just shown that the $^{[3]}$B triangles contain a significant fraction of NBOs and that the concentration of the former depends significantly on T, the overall concentration of NBOs does not depend strongly on temperature (see Fig. 4 in Part I). The reason for this is that, on one hand, we have three times more Si than B atoms, i.e., the strong T dependencies of $^{[3]}$B are not that relevant, and, on the other hand, some of the NBOs associated with $^{[3]}$B are probably accommodated by the Si atoms, thus weakening the T dependence of the overall NBO concentration. As a result, one can make an extrapolation of the T-dependent BO concentration to low temperatures and estimate that around T_g this value is slightly above 80%. This result agrees very well with the prediction of the YBD model, which foresees 80% and 20% for BO and NBO concentration, respectively, and also with results from ^{17}O NMR experiments [37].

For the BOs we have found that 45% belong to Si-O-Si bridges, 25% to Si-O-B bridges, and only 4% to B-O-B bridges. For the present composition, the YBD model predicts the presence of reedmergnerite, diborate, and pyroborate suprastructural units, and consequently there should be 47% Si-O-Si, 28% Si-O-B, and 5% B-O-B, in very good agreement with our findings. However, in the ^{17}O NMR experiments of Wang and Stebbins only a low concentration of Si-O-B has been found [37], which might imply that the Si and B networks are not perfectly mixed (see also [26,38]). Although such an nonideal mixing behavior is indeed compatible with our simulation data [we recall that in Part I, Fig. 6(b), we have shown that at small wave vectors the partial structure factor for Si-B indicates the presence of a demixing in the nano scale], the effect is so small that it does not affect the concentration of the Si-O-B connections, and hence this value can still be relatively elevated.

Finally, we mention that the possible connection of NBO to the $^{[3]}$B triangles makes that the latter can be separated into two classes [4]: The ones including one or two NBOs, called asymmetric units (labeled hereafter $^{[3]}$B$_a$), and the ones completely connected to the network through BOs, i.e., with zero NBOs, called symmetric units (labeled hereafter $^{[3]}$B$_s$). The YBD model does predict the relative concentration of these two units and for the current composition one should have 55% of $^{[3]}$B$_a$ and 45% of $^{[3]}$B$_s$. The corresponding values we have measured for our glasses are around 58% for $^{[3]}$B$_a$ and 42% for $^{[3]}$B$_s$; thus, they agree very well with the predictions of the YBD model, although our error bars for these concentrations are relatively large. In view that one has a strong cooling-rate dependence of the concentrations for $^{[3]}$B and $^{[4]}$B, this agreement might surprise. However, NMR experiments [26] have probed the cooling-rate dependencies for these two $^{[3]}$B structures and found that the concentration of $^{[3]}$B$_s$ is almost independent of this rate, whereas the ones of the asymmetric units shows a decrease of about 6% when the cooling rate was decreased over four orders of magnitude. Thus, we can conclude that the transformation of $^{[3]}$B into $^{[4]}$B units is mainly made by eliminating the $^{[3]}$B$_a$ structures. Unfortunately, the temperature dependence of $^{[3]}$B$_s$ and $^{[3]}$B$_a$ in the liquid state (shown in Fig. 2) does not allow us to confirm this conclusion since the error bars are too large.

In Fig. 1(d) of Part I we have seen that the first-nearest-neighbor peak in $g_{\rm OO}(r)$ is split into two. The reason for this feature is given in Fig. 4, where we have decomposed this correlation function into contributions from first-neighbor O-O distances in SiO_4, BO_3, BO_4, and SiO_5 units, the latter occurring with a probability of around 7%. From the graph we recognize that the peak at 2.40 Å is due to the O-O distance within the trigonal and tetrahedral boron structures, which give rise to peaks at 2.38 and 2.42 Å, respectively. These values agree well with the ones obtained from neutron-scattering experiments on B_2O_3 glass and on binary borate glasses containing modifiers for which, depending of the nature and concentration of the modifier, distances ranging from 2.38 to 2.42 Å are found [34]. For trigonal units, the present O-O distance agrees also with that extracted from classical MD simulations for B_2O_3 glass, which was 2.37 Å [39].

The main nearest-neighbor peak in $g_{\rm OO}(r)$ is found at 2.66 Å and its presence is entirely due to the SiO_4 tetrahedra. This distance is close to the one found in pure SiO_2 glass [40], but this does not imply that the geometry of this structural entity is not affected by the presence of other network-formers and/or modifiers. This coincidence is only due to the effect of averaging over distorted SiO_4 tetrahedra with short Si-NBO bonds and long Si-BO bonds (see Fig. 1 and Table I), as already reported in previous *ab initio* simulations for other silicates [19,21,22,41,42]. Finally, we mention that the O-O distance corresponding to the SiO_5 units is somewhat smaller than the one for the SiO_4 tetrahedra. Since only 2.5% of the defective SiO_5 structures are associated with a NBO, the reduced Si-O distance is not related to these NBO atoms.

From Figs. 2(a), 2(b), and 2(c) in Part I we see that also the PDFs for Si-Si, Si-B, and B-B show a split first-nearest-neighbor peak. A detailed inspection of these features shows that they are related to the presence of defective edge-sharing units and/or defective SiO_5 units which, due to the high quenching rate, are more abundant in our samples than in real glasses. This is also the case for the first peak in the B-B correlation: We have found it to be present only in one of the samples and therefore consider it to be atypical. The relevant peak in this PDF is located at 2.60 Å, which is in very good agreement with recent neutron scattering studies by Michel *et al.* [43], who found for the same composition as considered in the present work a distance of 2.64 Å, and *ab initio* simulations of B_2O_3, for which one finds 2.55 Å [44]. However, other neutron-scattering experiments have found that the peak is located between 2.77 and 2.85 Å for B_2O_3 and alkali-metal borate glasses with comparable alkali-metal content, respectively [34]. This shows that extracting such detailed information from neutron scattering experiments is not a trivial task.

We also point out that this distance might be affected by the high quench rate used in computer simulations. Since we have seen that our simulations predict a concentration of $^{[3]}$B that is too high, it can be expected that a smaller cooling rate (which will give rise to more $^{[4]}$B units) will lead to a B-B distance that is larger, since we have seen in Fig. 3 that the distance $^{[3]}$B-O is smaller than the $^{[4]}$B-O one. Finally, we mention that this too low concentration of $^{[4]}$B hinders us to check the validity of the so-called "tetrahedral boron avoidance" principle, i.e., the trend seen in NMR experiments that the $^{[4]}$B units have the tendency of not being nearest neighbor [45,46].

To understand how the alkali-metal atoms arrange around the BO_3 and BO_4 units, we show in Fig. 5 the corresponding PDF. One clearly sees that the nearest-neighbor peak (bold solid line) is the sum of two contributions. We have found that it is reasonable to decompose the main peak into B-Na pairs that share exactly one oxygen atom (thin solid line) or more than one O atom (thin dashed line). Thus, we recognize that the shoulder at around 3.25 Å is due to the B-Na pairs that share one oxygen atom, whereas the main peak, located at 2.77 Å, is produced by the pairs that share more than one oxygen. That sharing more than one oxygen leads to a shorter distance between the B-Na pairs is reasonable, since these oxygens give rise to an effective attraction between the cations.

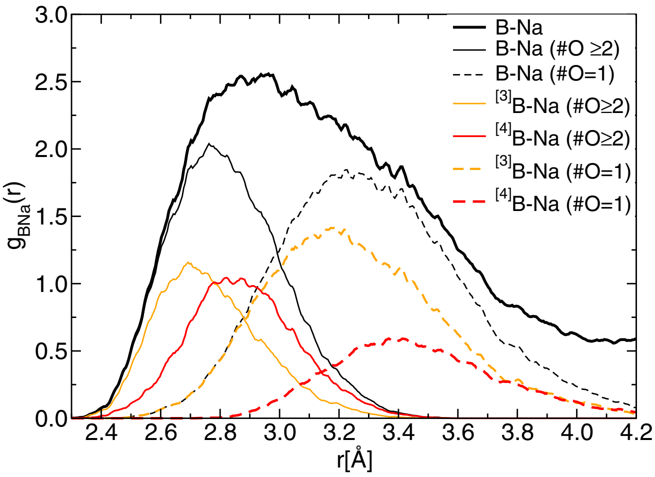

FIG. 5. (Color online) Decomposition of the first peak of the B-Na PDF for the glass according to boron coordination as well as to the number of oxygens that are shared between the B and Na atom.

The two mentioned peaks can be decomposed further into the contributions stemming from $^{[3]}$B and $^{[4]}$B. We find (see Fig. 5) that the $^{[3]}$B-Na distances are shorter than the one in $^{[4]}$B-Na, which is reasonable since the tetrahedral structures are larger than the trigonal ones. Furthermore, we recognize from this decomposition that the probability that a $^{[4]}$B shares exactly one oxygen atom with a Na is significantly smaller than the corresponding probability for a $^{[3]}$B. This result is related to the three-dimensional distribution of the Na atoms around the boron units, as we discuss next.

Since the PDFs give only information on the relative arrangement of two atoms it is instructive to consider also three-dimensional distribution functions. In particular, we are interested to understand how the Na atoms are arranged around the $^{[3]}$B and $^{[4]}$B structures. Since each $^{[3]}$B triangle or $^{[4]}$B tetrahedron will have a slightly different geometry, we have mapped each of them on an average structure. For the $^{[3]}$B we thus proceeded as follows: We translated each BO_3 triangle, together with its nearest Na, to a coordinate system in which the B is at the origin and the three O atoms define the x-y plane. In this plane we set up an equilateral triangle with the vertices at a distance 1.37 Å from the origin (i.e., the mean B-O distance found in the PDF) and with one of them lying on the y axis. This triangle defined our ideal reference structure. The real $^{[3]}BO_3$ triangles were then rotated in this plane such that the average squared distance of the real oxygens from the ideal positions (given by the reference structure) were minimized. (We note here that the four atoms of the $^{[3]}BO_3$ structure do basically lie in a plane and hence the reference triangle is a good approximation.) In order to exploit the symmetry of the trigonal structure we applied all possible symmetry operations to this triangle, carrying along the Na atoms. These last operations allow thus to improve the statistics regarding the regions in which the Na atoms prefer to be. In Fig. 6(a) we show the projection of this distribution onto the x-y plane and we see that the Na preferential region presents the expected threefold symmetry along the three BO bonds. We see that the center of the triangle is basically devoid of Na atoms; i.e., they prefer to arrange around the three B-O axes. Note that in the graph we distinguish the Na atoms that share one (crosses) and two (circles) oxygen atoms with the central B atom. These latter ones are found close to the angle bisector O-B-O and their distance from the B atom is slightly smaller than the former ones. Thus, this explains why the corresponding PDFs, shown in Fig. 5, have their maximum at different distances.

In panel (b) we show the projection of the distribution in the direction of the y axis. We show only the Na atoms that are nearest neighbor with the oxygen atom #1 and we distinguish again atoms that share one (circles) and two (crosses) oxygen atoms with the central B. We see that most of the latter atoms are close to the plane spanned by the three oxygen atoms and that the distribution of (all) the Na is quite circular around the axes defined by a B-O bond.

To generate panels (a) and (b) of Fig. 6, we have only used those $^{[3]}$B units which have three BOs as neighbors. There is, however, a substantial fraction of $^{[3]}$B's which have one NBO as nearest neighbor (58%) and hence can be expected to have an asymmetric distribution of Na atoms around them. That this is indeed the case as shown in Fig. 6(c), where we show these triangles (oriented such that the NBO points upward). From

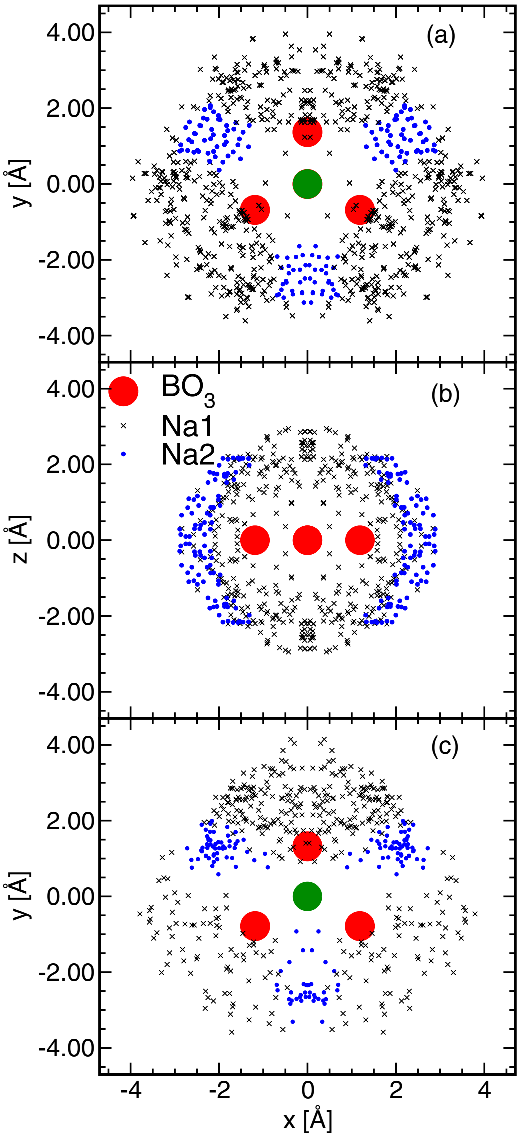

FIG. 6. (Color online) Distribution of the Na atoms around a BO_3 unit. The crosses and circles show Na atoms that share, respectively, exactly one and two oxygen atom(s) with the central B atoms. (a) BO_3 in top view (the oxygen on the top defines oxygen #1). (b) BO_3 in side view. Only Na atoms that are nearest neighbor to the oxygen atom #1 (at the center) are shown. (c) The asymmetric BO_3 unit with two BO and one NBO (oxygen #1, on top).

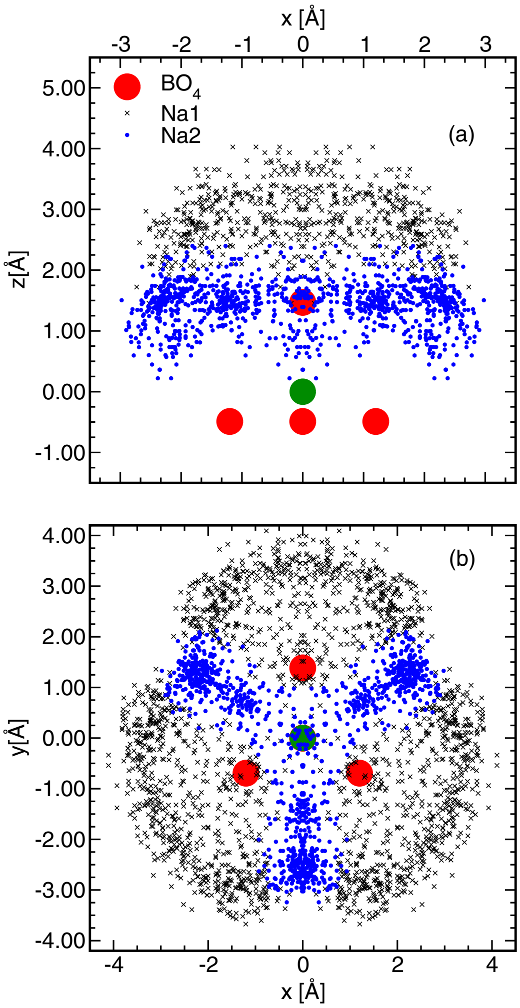

FIG. 7. (Color online) Distribution of the Na atoms around a BO_4 tetrahedron. (a) Top view. Only the Na atoms that are first-nearest neighbor of oxygen #1 (the top one) are shown. (b) Bottom view. Only the Na atoms that are *not* nearest neighbor of oxygen #1 (at the center) are shown.

the snapshots we clearly see that the NBO has significantly more Na around it: We have found on average 3.1 Na instead of the 1.3 Na found around the BO of the same asymmetric $^{[3]}$B unit. The latter value is comparable with the average number of Na around a BO in a *symmetric* $^{[3]}$B unit, which is equal to 1.2. The total number of Na atoms around a $^{[3]}$B with one NBO is equal to 4.8, which has to be compared with 3.2 Na around a *symmetric* $^{[3]}$B unit. Note that these average total values are lower than the sums over the individual BO and NBO values due to the presence of Na atoms, which are shared by two oxygens.

To study the distribution around the $^{[4]}$B units, we have applied three rigid rotations to each of the real tetrahedra so that its vertices were as close as possible to the ones of a regular tetrahedron that had a BO distance equal to 1.47 Å (i.e., the average bond lengths extracted from the first peaks of the PDFs for the tetrahedra) with one vertex pointing in the z direction. In order to exploit the symmetry of the structure, we applied again all possible symmetry operation to this tetrahedron, carrying along the Na atoms.

In Fig. 7(a) we show the projection of the distribution onto the x-z plane. For the sake of clarity we show only those Na atoms that are nearest neighbors of the oxygen atom shown at the top (e.g., O#1). We distinguish again between Na atoms that share exactly one (crosses) or two (circles) oxygen atom(s) with the central B atom. An inspection of the distribution around the O#1 as projected on the x-y plane (not shown) demonstrates that the former Na's have a (basically) circular distribution around the B-O axis, whereas the latter Na's (circles) have a distribution with a threefold symmetry. This symmetry can be clearly recognized from Fig. 7(b), where we plot the Na distribution projected onto the x-y plane. (Note that in this panel the distribution is seen from the bottom of

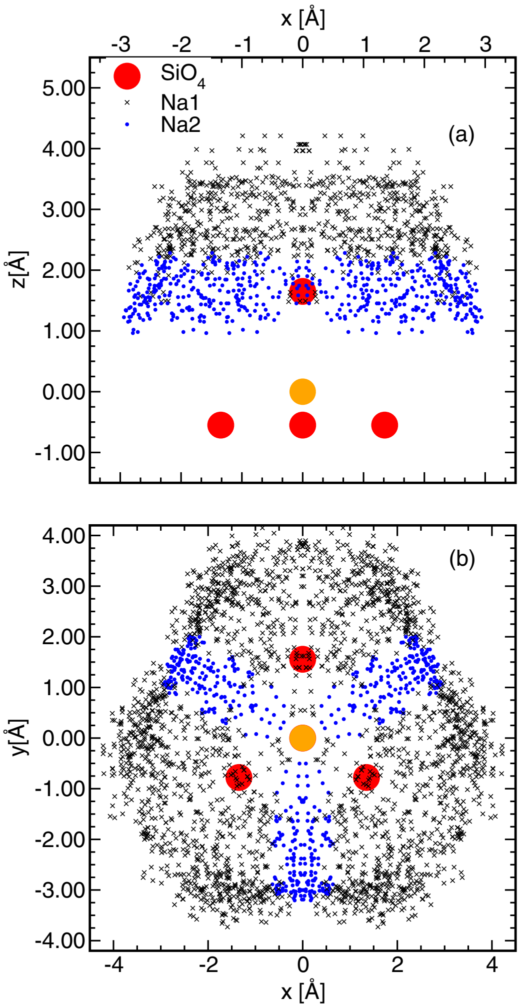

FIG. 8. (Color online) Distribution of the Na atoms around a SiO_4 tetrahedron. (a) Top view. Only the Na atoms that are first-nearest neighbor of oxygen #1 in the top are shown. (b) Bottom view. Only the Na atoms that are *not* nearest neighbor of oxygen #1 are shown.

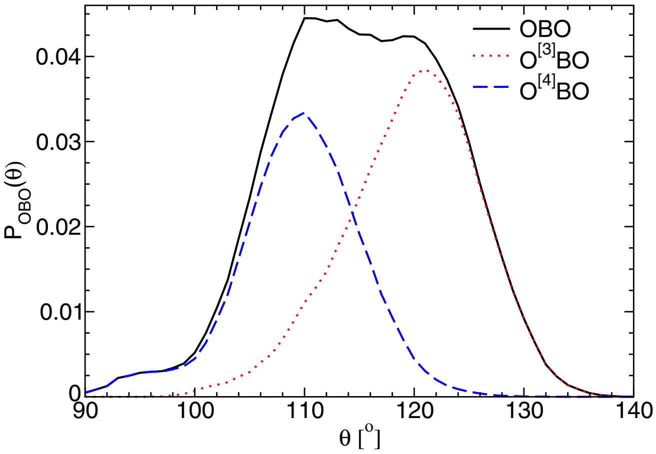

FIG. 9. (Color online) Distribution of the bond angle O-B-O and its decomposition into $O^{[3]}BO$ and $O^{[4]}BO$ components.

the tetrahedron and that the Na atoms that are first-nearest neighbor of oxygen #1, located on the positive z axis, are *not* shown.) From the two projections we also recognize that the Na atoms that share two O with the central B typically have distances that are smaller than those Na atoms that share only one, in agreement with the corresponding PDFs shown in Fig. 5.

Since the BO_4 unit have the same symmetry as the SiO_4 tetrahedra, it is instructive to compare the Na distribution around these two structures. For this we show in Fig. 8 the distribution for SiO_4. (Here we have used the value 1.65 Å for the Si-O distance of the reference tetrahedron and in order to make the graphs comparable we show in the graphs the same number of Na as in Fig. 7.) The comparison with the corresponding distribution for BO_4 shown in Fig. 7 reveals that for the case of SiO_4 the Na atoms are concentrated more around the axis between the cation and the oxygen, thus making that the number of sodium atoms that share only one oxygen with the central cation (crosses) is significantly higher. Furthermore, we see that the Na which share two oxygen atoms with the central cation (circles) are spread over a significantly larger portion of space for the case of BO_4. This result is reasonable since the boron atoms have a smaller effective charge than the Si atoms, thus restricting the Na atoms less. Hence, we see that, due to the effect of charge balance, the distribution of Na atoms around the two tetrahedral structure shows small but significant differences.

B. Bond angle distributions in NBS glass

Complementary and additional information on the local ordering and organization of the glass network is obtained from the analysis of the bond-angle distributions (BADs) $P_{\alpha\beta\gamma}(\theta)$ and these nine distributions are shown in Fig. 9 of Part I [10]. As expected, with decreasing temperature these distributions become narrower and some of their features more pronounced. At 300 K the distribution $P_{\rm OSiO}(\theta)$, Fig. 9(a) in Part I, shows a quite narrow distribution with a peak at about 108°, very close to the ideal intratetrahedral O-Si-O angle, and thus similar to the geometries found for pure SiO_2 and in alkali silicate glasses [19–22]. A closer inspection of this distribution reveals the presence of a small bump at about 90°, which is the fingerprint of defective fivefold coordinated Si and/or edge-sharing tetrahedra.

The distribution $P_{\rm OBO}(\theta)$ shown in Fig. 9(b) of [10] is broader than $P_{\rm OSiO}(\theta)$ and, in fact, one sees that it is the sum of two peaks. (The shoulder at around 95° is due to edge-sharing triangles/tetrahedra, geometries that can be expected to vanish if the cooling rate is decreased.) In Fig. 9 we demonstrate that these peaks are related to the presence of O-$^{[3]}$B-O and O-$^{[4]}$B-O, giving rise to distributions that have a maximum at around 121° and 110°, respectively. These values are close to the expected values for an isosceles triangle (120°) and an ideal tetrahedron (109°). (We recall that the $^{[3]}BO_3$ triangles are basically planar, similar to the case of pure B_2O_3 glass [47].) In addition, we see that the distribution for the angles O-$^{[3]}$B-O is asymmetric in that it has a tail to smaller angles. This feature is related to the presence of $^{[3]}$B that have a NBO, thus making that the triangular unit has two angles NBO-B-BO at around 123° and a smaller one (BO-B-BO) at around 113°.

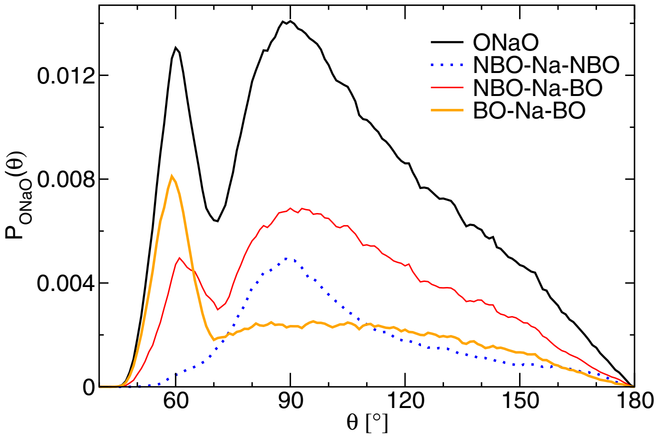

FIG. 10. (Color online) Distribution of the bond angle O-Na-O and its decomposition into BO and NBO.

Figure 10 shows the angle distribution $P_{\mathrm{ONaO}}(\theta)$. In Sec. III C of Part I [10], we showed that this double-peak structure becomes more pronounced if temperature is decreased (see Fig. 9(c) in [10]). In agreement with previous results from *ab initio* simulations for low-silica alkali-alkaline earth melts [42], we see that the peak at around 60° is related to the BO-Na-BO angle, whereas the one at 90° to the NBO-Na-NBO angle. Finally, the distribution for the BO-Na-NBO has peaks at the two angles. Since NBOs are basically absent in the $^{[4]}\mathrm{BO}_4$ units, the two latter distributions can thus be associated with Na atoms that are around $Q^{(3)}$ and $^{[3]}\mathrm{BO}_3$ units. Since the concentration of the $^{[3]}\mathrm{BO}_3$ units is decreasing with decreasing T and the one of $Q^{(3)}$ is increasing (see Fig. 4 in [10]), it is at this point difficult to estimate how the distribution P_{ONaO} will be in glasses that have been produced with the cooling rates used in real experiments.

Further insight into the connectivity of the network-formers can be obtained from the BAD centered on the BOs, i.e., the angular distributions Si-O-Si, B-O-B, and Si-O-B, shown in Part I, in Figs. 9(d), 9(e), and 9(i), respectively. All three distributions present small peaks located at 93°, 84°, and 87°, respectively, indicating the presence of the defects mentioned in the previous subsections (SiO_5 and edge sharing). Therefore, it can be expected that with decreasing cooling rate these peaks disappear [see Fig. 5(b) in Part I] and are not present in glasses obtained with cooling rates accessible in real experiments. For the intertetrahedral angle Si-O-Si, the distribution shown in Fig. 9(d) of Part I has a maximum around 130°, and a comparison to the corresponding data for pure SiO_2 glass shows that this position is shifted to smaller angles due to the sodium atoms, in agreement with results for a sodium silicate glasses [19]. Finally, we notice that both P_{SiONa} and P_{BONa} distributions [see Figs. 9(g) and 9(h) in Part I] have maxima around 90° and present a significant decrease of the probability at large angles when T is decreased. These modifications are related to the fact that Na is avoiding the direction of the Si-O bond (or B-O bond) as can be seen, for example, in Fig. 6 for the trigonal units. The maxima around 90° are probably related to the angles corresponding to Na which share two oxygen atoms with the central cation (blue circles in Figs. 6–8).

Before we conclude this section on the structural properties of the glass, we mention that we have not found any boroxol rings in our sample, and this despite the relatively large concentration of $^{[3]}$B units. Thus, in contrast to pure $\mathrm{B}_2\mathrm{O}_3$ glass in which these rings are relatively frequent [48], the presence of a second network former Si and the network modifier Na make that these rings are no more favorable structural units, at least in a compositional range with a low content of $\mathrm{B}_2\mathrm{O}_3$.

In this section, we have presented an analysis of the three local structural units present in the glass, i.e., $^{[3]}$B triangle, $^{[4]}$B, and SiO_4 tetrahedra, characterizing them by means of their bond lengths and angles distributions. In particular, we have studied the spatial distributions of the Na atoms around these structural units and have found that they present different characteristic geometric features that depend on the network-former type (B or Si), the coordination ($^{[3]}$B or $^{[4]}$B), as well as on the oxygen species (BO or NBO) they are connected with.

IV. VIBRATIONAL PROPERTIES

In order to study the vibrational properties of the NBS glass we have relaxed its structure to 0 K and then determined the dynamical matrix. This was done with a finite difference scheme using atomic displacements of about 2.6×10^{-3}Å. The diagonalization of the dynamical matrix gave then the $3N$ eigenvalues $\{\omega_p\}$ as well as the corresponding normalized eigenvectors $\{\mathbf{e}(\omega_p)\}$, for $p = 1, 2, \ldots, 3N$, where N is the total number of atoms in the sample, i.e., 320 in our case. The vibrational density of states (VDOS) is then given by

$$g(\omega) = \frac{1}{3N-3}\sum_{p=4}^{3N}\delta(\omega-\omega_p), \quad (1)$$

and it is shown in Fig. 11(a). It is also instructive to decompose the VDOS into the so-called partial-VDOS, i.e., the contributions from the different species,

$$g_\alpha(\omega) = \frac{1}{3N-3}\sum_{p=4}^{3N}\sum_{I=1}^{N_\alpha}\sum_{k=1}^{3}|\mathbf{e}_{I,k}(\omega_p)|^2\delta(\omega-\omega_p), \quad (2)$$

where $\alpha =$ Si, O, Na, and B and $\mathbf{e}_{I,k}(\omega_p)$ is that part of the eigenvector $\mathbf{e}(\omega_p)$ that contains the three components of particle I. The so-obtained discrete vibrational spectra has been broadened with a Gaussian of full width at half maximum of 30 cm^{-1} and they are included in Fig. 11(a) as well.

The figure shows that in the total VDOS one can identify four main bands: a first one which ranges from 0 to ≈600 cm^{-1}, a second one between 600 and 820 cm^{-1}, a third one between 820 and 1200 cm^{-1}, and finally the fourth one between 1200 and 1600 cm^{-1}. Inspection of the partial VDOS shows that the four elements contribute in very different ways to these four bands. For the band at the lowest frequencies we see that the Na atoms give rise to the marked peak at around 180 cm^{-1} and that the oxygen atoms contribute significantly in the whole frequency range of this band, whereas the contributions of the Si and B are relatively weak. These results are in qualitative agreement with the ones obtained for sodium and lithium silicate glasses [21,49].

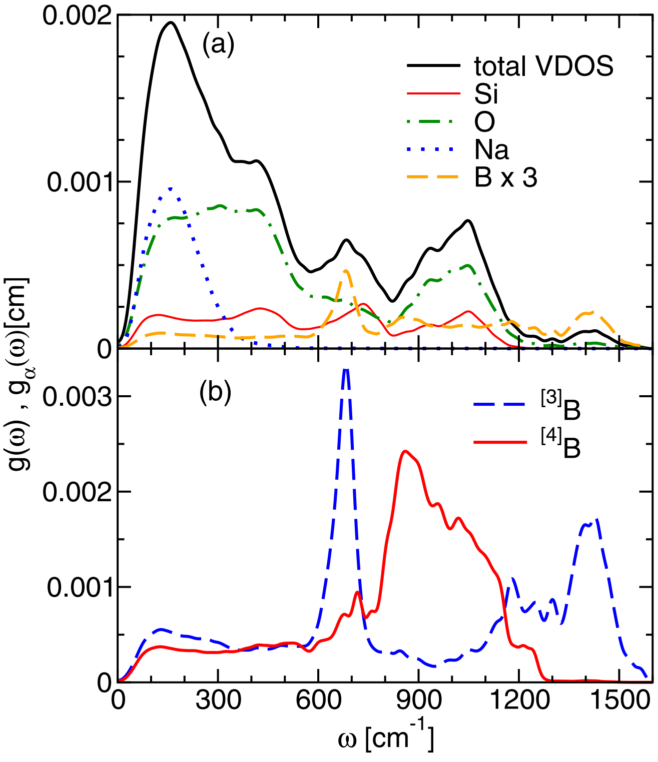

FIG. 11. (Color online) (a) Total and partial VDOS for the glass. The total VDOS is normalized to 1, and the partial VDOS of boron is multiplied by 3 in order to enhance its visibility. (b) Partial VDOS for trigonal $^{[3]}$B and tetragonal $^{[4]}$B boron atoms. Both are normalized to 1 in order to allow a better comparison.

For frequencies below 1200 cm^{-1}, one finds that the partial VDOS of Si and O present three main bands, as in pure silica [40,50,51]. However, their features (position, width, and intensity) are somewhat modified due to the presence of Na and B. For example, in pure silica one finds a prominent peak at around 800 cm^{-1} which is related to Si [51], and our data show that this peak is shifted to lower frequencies and has an intensity similar to the one of the band below 600 cm^{-1}, whereas in pure silica it is two times more intense. The so-called high-frequency band in pure silica located above 1000 cm^{-1} [51] is also shifted to lower frequencies and this can be rationalized by recalling that the modes on the left side of this band can be attributed to the softening of stretching motions in silicates due to the depolymerization [52].

The presence of B in the system gives rise to a peak at around 680 cm^{-1} and the band at the highest frequencies. (In the latter one finds also contributions of the oxygen atoms that are connected to B atoms.) These results agree with interpretations of Raman and hyper-Raman experiments for alkali borates or borosilicate glasses and melts [9,53,54] and are also supported by *ab initio* modeling of vibrational spectra (VDOS, infrared, Raman, and hyper-Raman) for B_2O_3 glass [47,48]. Due to the importance of the $^{[3]}$B and $^{[4]}$B units, it is useful to decompose the partial VDOS of the boron atoms into contributions that come from these two motifs, and in Fig. 11(b) we show the two spectra. Note that in order to facilitate the comparison of the two curves we have normalized them to one. Since we have found a strong T dependence of the concentration of the $^{[3]}$B and $^{[4]}$B units this normalization also makes it possible to infer how the real spectra would look if we would use a cooling rate that corresponds to the one in real experiments, i.e., glasses with a concentration of $^{[3]}$B around 30% (see Sec. III A). (Here we assume that the main effect of the cooling rate is the concentration of the $^{[3]}$B and $^{[4]}$B units and hence the other partial VDOS are affected only weakly.)

For frequencies below 600 cm^{-1} the spectra for the $^{[3]}$B and $^{[4]}$B units are very similar and hence this part of the spectrum should not be affected by cooling-rate effects. At higher frequencies we find that the vibration of the trigonal boron gives rise to a pronounced peak at around 680 cm^{-1} and a broad band between 1100 and 1500 cm^{-1}. This result might be in contrast to the interpretation of Raman spectra in which one relates the peak in the 600–700 cm^{-1} region to the presence of reedmergnerite and/or danburite rings containing tetrahedral borons [8,9,29]. Indeed, we see from our spectra that the $^{[4]}$B units do not have a significant contribution at these frequencies (their vibrational modes are mainly located in a band between 800 and 1200 cm^{-1}). Nevertheless, we cannot conclude that this experimental interpretation of the origin of the peak is incorrect, as in our decompositions we have considered only the modes of the borons atoms in trigonal and tetrahedral units and not the modes of the whole reedmergnerite and/or danburite rings. Finally, we mention that the distinct features in the spectrum of the $^{[3]}$B and $^{[4]}$B units make it possible to infer from the experimental spectrum the concentration of these units in the sample.

The vibrational features of the various atoms and species depend not only on the number of their neighbors but also on how the latter are connected to the rest of the network. As discussed above, for the trigonal boron atoms one can therefore distinguish between the symmetric units ($^{[3]}$BO units completely connected to the network through BO atoms) and the asymmetric units (boron atoms that have at least one NBO as nearest neighbor). In Fig. 12(a) we show the VDOS for these two subunits and we recognize that the peak around 680 cm^{-1} has contributions from symmetric as well as asymmetric $^{[3]}$B units and that the peak of asymmetric units is more pronounced.

Also interesting is the high-frequency band above 1100 cm^{-1} since the decomposition shows us that it is the sum of three peaks: two peaks located at around 1050 and 1450 cm^{-1}, which correspond to the modes of the asymmetric $^{[3]}$B, and a broad peak located in between and which is related to the vibrational motion of the symmetric $^{[3]}$B units. Although we have not investigate the details regarding what type of motion corresponds to these three peaks, it is likely that they can be to attributed to complex stretching motions as it has been suggested, for example, from IR experimental data for AgI-doped borate glasses [55].

The decomposition of the $^{[4]}$B modes taking into account the nature of the second network-former to which the BO_4 unit is linked is shown in Fig. 12(b). (We recall that the large majority of $^{[4]}$B have only BO as nearest neighbors.) Among the $^{[4]}$B units present in our structures, the concentration of the reedmergnerite and danburite suprastructural units [8] (labeled $^{[4]}B_{Si_4B_0}$ and $^{[4]}B_{Si_3B_1}$, respectively) dominates and

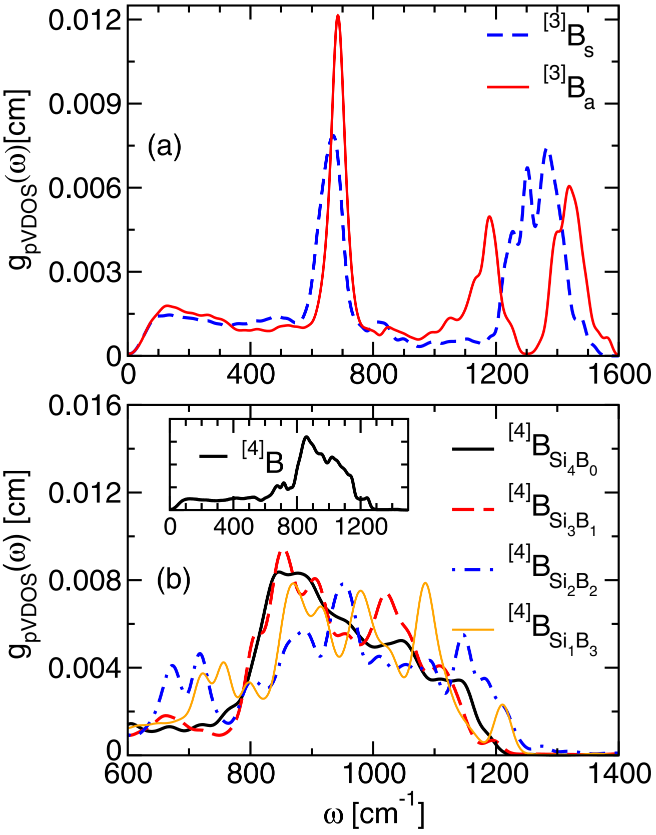

FIG. 12. (Color online) Partial vibrational of state for boron. (a) Decomposition of the pVDOS for $^{[3]}$B into contributions from the symmetric and asymmetric trigonal environments $^{[3]}B_s$ and $^{[3]}B_a$. (b) Decomposition of the pVDOS for $^{[4]}$B into contributions related to different types of second-nearest neighbors.

is around 43% and 27%, respectively. We see that these two structures give rise to a very similar partial VDOS with a asymmetric band above 800 cm^{-1}. This result may contradict the interpretation of recent Raman investigations in which the modes of the reedmergnerite and danburite suprastructural rings were assigned to a different spectral band, between 600 and 700 cm^{-1} [8,9,29]. However, as stated above, one has to recall that our assignments are based regarding the modes of tetrahedral borons and not of the rings to which they belong, as done in experimental studies which make use of analogies to the experimental spectra of reedmergnerite and danburite crystals. For the structural units $^{[4]}B_{Si_2B_2}$ and $^{[4]}B_{Si_1B_3}$, we find that the band above 800 cm^{-1} is more symmetric, but now we find also modes at around 700 and 750 cm^{-1}, respectively. Hence, our analysis gives evidence that this spectral band can give information on the nature of the second-nearest neighbor. However, due to the rather poor statistics of the present simulation, it is hard to draw more quantitative statements. Finally, we recall that silicate glasses show at low frequencies a spectral feature, known as Boson peak, the origin of which has been in the focus of interest of many investigations [56,57]. However, since the size of our simulation box is small, these low-frequency excitations are not accessible since their associated length scale is comparable to size of our simulation box and it is known that, at low frequencies, the VDOS results are strongly affected by finite size effects [58]. Hence, we cannot comment on the nature of this peak for the present system.

In this section, we have presented an analysis of the vibrational modes present in the NBS glass by identifying the vibrational signatures of the atomic species and local structural units. The contributions of boron atoms have been studied in detail, and we have identified the particular features of $^{[3]}$B and $^{[4]}$B units, as well as those of symmetric and asymmetric $^{[3]}$B units.

V. ELECTRONIC PROPERTIES

In this section we analyze the electronic properties of our NBS glass samples in terms of the electronic densities of states and the Bader charge variations.

A. Electronic density of states

To calculate $D(E)$, the average total electronic density of states (eDOS), we have in a first step used the KS energies obtained for each 0 K relaxed structure to determine the partial eDOS $D^l_\alpha(E)$ for $\alpha =$ Si, O, Na, B and the angular momenta $l = 0, 1$. Subsequently, $D(E)$ has been obtained as $D(E) = \sum_\alpha c_\alpha \sum_{l=0,1} D^l_\alpha(E)$, where c_α is the concentration of species α.

In Fig. 13 we show $D(E)$ as well as the partial eDOS, $D^l_\alpha(E)$, for $\alpha =$ Si, O, Na, B and $l = 0, 1$. Just above the Fermi level, $E = 0$, we find a band gap of approximately 3 eV. Although to our knowledge experiments have not

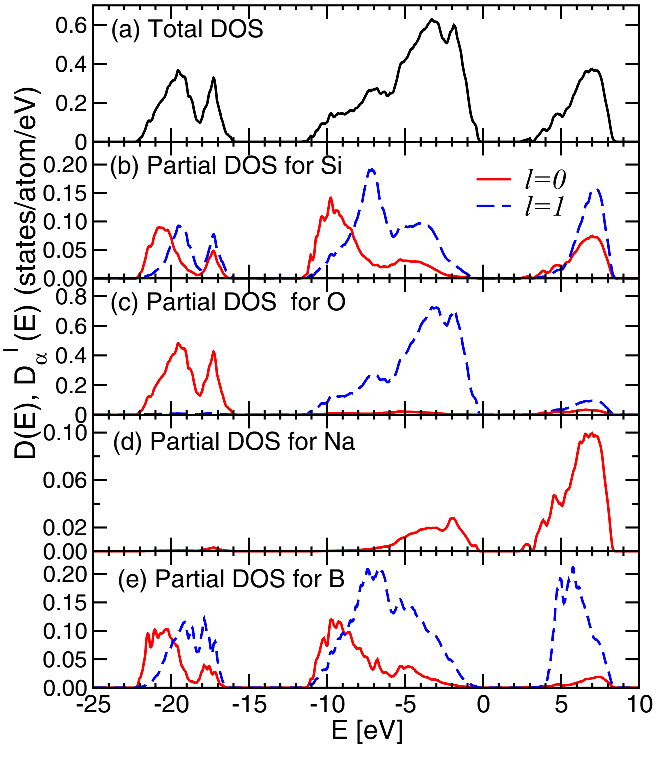

FIG. 13. (Color online) (a) Total eDOS $D(E)$ in the glass. (b)–(e) Partial eDOS $D^l_\alpha(E)$ for $\alpha =$ Si, O, Na, and B. The solid and dashed lines show $D^l_\alpha(E)$ for $l = 0$ and $l = 1$, respectively. The origin of the energy is the Fermi level.

yet determined the value of this gap for NBS glasses, we can compare it to values for other glasses. For the case of $\mathrm{SiO_2}$, DFT calculations have predicted values around 5 eV [21,59,60], whereas for sodium and lithium silicates the width of the gap was found to be smaller: 3.4 eV for the lithium disilicate [21] and ranging between 2.77 and 2.86 eV for sodium tetrasilicate [19]. This narrowing of the gap has been argued to be related to the presence of the Na and Li atoms, and the same explanation is likely to hold also for our NBS composition which presents a high soda content. However, when making these arguments one should not forget the well-known problem of standard DFT calculations, namely that they typically predict gaps that are substantially smaller than the experimental ones, for both semiconductors and insulators [61].

Below the Fermi level, $D(E)$ shows two valence bands: a first one between -22.28 and -15.96 eV and a second one between -11.64 and 0 eV. The low-energy band is also observed in the partial eDOS for Si, B, and O and it has a double-peak structure. Since the peak at higher energy, $E \approx -17$ eV, is absent in fully connected networks such as pure $\mathrm{SiO_2}$ and $\mathrm{B_2O_3}$, we can assign it to electronic states of Si and B atoms which have at least one NBO, in agreement with results for lithium silicate crystals and glasses [21,62], as well as for a sodium silicate glass [19]. We also note that for Si and B this double-peak structure is present for $l = 0$ and $l = 1$, thus indicating a hybridization of their respective $2s$ and $2p$ states with each other.

The features of the valence band at energies above -11 eV can be understood by recalling the ones observed in pure $\mathrm{SiO_2}$ and $\mathrm{B_2O_3}$ glasses [44,59], in spite of the presence of a small contribution in $D^l_{\mathrm{Na}}(E)$ [see Fig. 13(d)]: The band between -11 and -5 eV may be assigned to contribution from bonding states between O $2p$ orbitals and Si sp^3 hybrids on one hand and with hybridized $2s$ and $2p$ orbitals of B atoms on the other hand. Finally, there is a large peak above -5 eV which originates mainly from O $2p$ since in this energy range the contributions from $D^l_{\mathrm{Si}}(E)$ and $D^l_{\mathrm{B}}(E)$ are substantially smaller. This peak is generally assigned to lone-pair O nonbonding $2p$ states [44,59].

B. Bader charges

Since simulations within a DFT approach make it possible to calculate the electronic properties of the system, one can correlate these with the local structure. In the present study we have employed the method proposed by Bader [63], which is also called "atom in molecule." In this approach one partitions the charge density into regions around each nucleus, the so-called Bader volume, using as boundary surfaces with zero flux; i.e., perpendicular to this surface the change density $\rho(\mathbf{r})$ is in a minimum: $\nabla\rho(\mathbf{r}) \cdot \mathbf{n} = 0$ [62,64]. The charge is then given by

$$Q^{\mathrm{Bader}}_{\alpha} = Z_{\alpha} - \int_{\mathrm{Bader\ volume}} \rho(\mathbf{r})dV, \qquad (3)$$

where Z_{α} is the number of electrons of an atom of type α.

We have found that the so-obtained charges are basically Gaussian distributed and hence they can be characterized by their mean value and width. The average Bader charge of silicon, oxygen, boron, and sodium atoms, as well as those of various species present in the structure of the NBS liquid at 2200 K and in the glass at 0 K, are listed in Table II. We recognize that these charges are quite different from the nominal valence charges (i.e., $+4$ for Si, -2 for O, $+1$ for Na, and $+3$ for B), which indicates a mixed ionic-covalent nature of the interactions. In the liquid, the absolute values of the charges are smaller than in the glass state, and their standard deviations are larger, which shows that in the liquid state there is a higher degree of disorder than in the glass state, in agreement with our analysis of the structural quantities and results of previous *ab initio* simulations [21]. For Si we see that the charge of the $Q^{(n)}$ species increases with n, a trend that has been termed "nonlocalized effect" of the sodium atoms [65,66] and which has also been found in other glassy and crystalline silicates [19,21,62].

For the borons we see that the charge depends on their coordination number, with the $^{[4]}$B being more positive than the $^{[3]}$B. This result is consistent with the observation that the former structure is surrounded by fewer Na atoms than the latter one (if one considers the number of Na per BO).

Regarding the oxygen species, we find that the BOs are slightly more negative that the NBOs, in both glass and liquid states. Note that a formal charge neutrality requires a more negative charge of NBOs, and previous DFT calculations on sodium and lithium silicates having NBOs [19,21,62] have indeed shown this to be the case. In fact, this failure of the Bader method to describe the different ionicity of Si-BO and Si-NBO bonds has already been pointed out for lithium disilicate [21,62], as well as in DFT calculations on clusters representing siliceous zeolites [67], and it originates from the partitioning scheme of the total electron density.

VI. DIELECTRIC PROPERTIES

A. Born charge tensors

Another possibility to associate an effective charge to a given atom I is to measure the force $\vec{F}^I$ that an external electric field $\vec{\mathcal{E}}$ induces on the atom [68]. For this so-called Born effective charge, one thus measures the tensor

$$Z_{I,ij} = \frac{\partial F^I_i}{e\partial \mathcal{E}_j} \quad I = 1,2,\ldots,N, \quad i,j \in \{x,y,z\}, \qquad (4)$$

where e is the elementary charge. Since on average our the system is isotropic, and we have indeed found that the ensemble average values of the off-diagonal elements of this tensor are negligible, one can define the average Born charge Z as a third of the trace of $Z_{I,ij}$: The so-obtained charges are listed in Table III. If one compares these values with the corresponding Bader charges (see Table II), one sees that most of them agree within the standard deviation. The notable exception is Na, for which the Born charge is significantly higher than the Bader charge ($1.063e$ vs $0.822e$). This difference can be rationalized by the fact that the sodium atoms are relatively mobile and hence will show a significant susceptibility, i.e., high effective charge, when an external field is applied.

For the sake of comparison we have included in the table also the values of the charges for pure silica glass (Si, O,

TABLE II. Average Bader charges for atoms and various species found in NBS liquid at 2200 K and in the glass at 0 K. In parentheses we give the standard deviations of the Gaussian distribution.

Charge [$\|e\|$]	Si	$Q^{(4)}$	$Q^{(3)}$	$Q^{(2)}$
Liquid	3.097(0.057)	3.122(0.046)	3.086(0.054)	3.075(0.049)
Glass	3.146(0.021)	3.159(0.018)	3.137(0.017)	3.113(0.012)
	O	BO	NBO	TBO
Liquid	−1.560(0.047)	−1.580(0.036)	−1.510(0.033)	−1.575(0.059)
Glass	−1.584(0.031)	−1.597(0.021)	−1.540(0.014)	−1.607(0.011)
	B	$^{[3]}$B	$^{[4]}$B	Na
Liquid	2.285(0.050)	2.277(0.069)	2.303(0.052)	0.822(0.024)
Glass	2.328(0.027)	2.308(0.020)	2.346(0.019)	0.830(0.027)

BO), as obtained in Refs. [40,69]. We recognize that for O and BO these charges are quite similar to the ones of the NBS glass, thus showing that the presence of the additional elements B and Na does not change these values in a significant manner. A larger difference is found for the charge of the Si atoms which for the case of NBS is smaller than the one in pure SiO_2. This decrease is likely related to the fact that the local environment of Si has changed from an almost perfect tetrahedral coordination to a distorted tetrahedral one, due to presence of NBO atoms and Na neighborhood.

B. Correlation between Born charges and structural features

The knowledge of the structure and local charges allows us to investigate the correlation between these two quantities. That such correlations do exist has, e.g., been demonstrated for the case of silica for which it has been found that the oxygen Born charge decreases as the corresponding Si-O-Si angle increases [40,69]. Since in NBS one has a much richer variety of local environments, it is of interest to see whether also for this system one can find correlations between the charge of an atoms and its local structure.

First we investigate the relationship between the NBOs Born charge and the associated bond length T-NBO, where T is the network-former: T = Si, $^{[3]}$B, and $^{[4]}$B; see Fig. 14. We see that there is indeed a significant correlation between these two quantities in that the (absolute) value of the charge increases with increasing distance, a result that is reasonable since with increasing distance the charge on the atom becomes less screened. This correlation can be fitted well with a linear function and hence we can write

$$Z_{\mathrm{NBO}}^{\mathrm{Si}}[e] = -2.10e[\text{Å}^{-1}] \times r_{\mathrm{Si-NBO}}[\text{Å}] + 1.86\,e, \qquad (5)$$

$$Z_{\mathrm{NBO}}^{\mathrm{B}}[e] = -2.16e[\text{Å}^{-1}] \times r_{\mathrm{B-NBO}}[\text{Å}] + 1.41\,e. \qquad (6)$$

TABLE III. Average Born charge for the Si, O, Na, and B atoms. (In parentheses are the standard deviations.) Also listed are the charges found in SiO_2 from Refs. [40,69].

	NBS	SiO_2 [40]	SiO_2 [69]
Si	2.996(0.198)	3.298(0.102)	3.177(0.121)
O	−1.591(0.099)	−1.649(0.062)	−1.588(0.078)
BO	−1.634(0.074)	−1.649(0.062)	−1.588(0.078)
NBO	−1.472(0.043)		
Na	1.063(0.035)		
B	2.142(0.245)		
$^{[4]}$B	2.398 (0.179)		
$^{[3]}$B	2.009 (0.153)		

Note that the very few NBO that are bounded to a $^{[4]}$B (red crosses) fall more of less on the same line as the ones connected to a $^{[3]}$B (blue triangles) which shows that this linear relation does not depend strongly on the environment of the boron atom. Furthermore, we see that also the slope for the data for T = Si is very close to the one for T = B from which we can conclude that the distance dependence of the NBO charge is independent of the atom to which the oxygen is attached (apart from a constant).

For BOs we have investigated the correlation between Z_{BO} and the bond angle spanned by the two bonds to its nearest neighbors (see [69] for a similar analysis in the case of silica). This correlation is shown in Fig. 15 (crosses) and we see that the charge depends linearly on the angles Si-O-Si and Si-O-B. The linear fits shown in the figure are given by

$$Z_{\mathrm{BO}}^{\mathrm{Si-O-Si}}[e] = -0.0035e[\mathrm{deg}^{-1}] \times \theta_{\mathrm{Si-O-Si}}[\mathrm{deg}] - 1.186\,e \qquad (7)$$

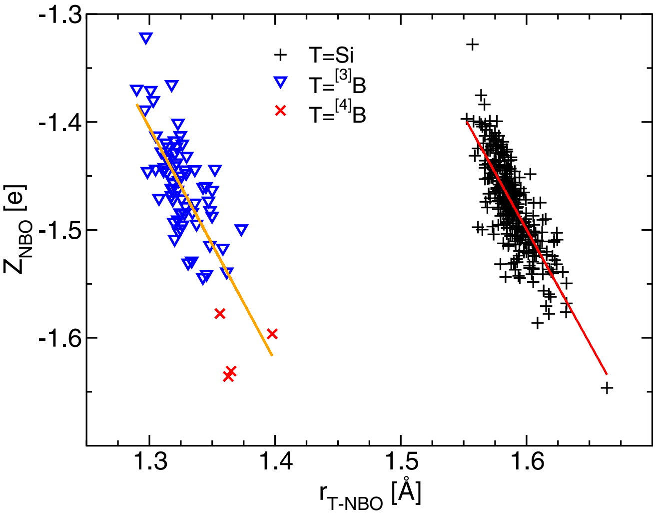

FIG. 14. (Color online) Dependence of the trace of the Born charge tensor Z_{NBO} for a NBO atom on the bond length with the network-former T for T = Si, $^{[3]}$B, and $^{[4]}$B . The straight lines are the linear fits with the expressions given in Eqs. (5) and (6).

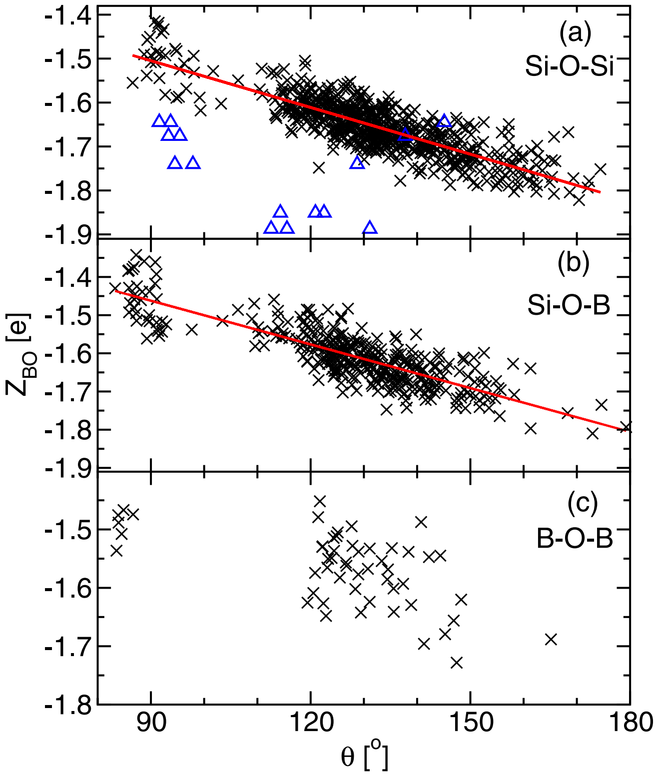

FIG. 15. (Color online) Dependence of the trace of the Born charge tensors Z_{BO} for a BO atom on its bond angle with the two network-formers: (a) Si-O-Si, (b) Si-O-B, and (c) B-O-B. The straight lines are the linear fits with the expressions given by Eqs. (7) and (8). The blue triangles in panel (a) are the oxygen triclusters.

and

$$Z_{\mathrm{BO}}^{\mathrm{Si-O-B}}[e] = -0.0038e[\mathrm{deg}^{-1}]\times\theta_{\mathrm{Si-O-B}}[\mathrm{deg}] - 1.119\,e. \tag{8}$$

Thus, we see that, within the accuracy of the data, the two slopes are the same and only the mean value of the charge is slightly different. Also included in panel (a) are the charges/angles for oxygen triclusters (blue triangles). We see that these charges are, on average, significantly more negative than the ones for BO and that they do not follow the linear relation given by Eq. (7) and hence they have not been considered in this fit.

In all three panels we see some data points at angles around 90°. These are related to defective structures that are present because of the high quench rate and hence should not exist in the real glass [see panels (d) and (e) of Fig. 9 in Part I]. Interestingly enough, the linear fits give a good description also of these defective structures, thus showing that the relation between angle and charge is rather general. Finally, we mention that for the B-O-B angle we do not find a significant correlation between the angle and the charge, at least if we do not take into account the defective structures with angles around 90°. (Note that the observed range in the value of this angle is smaller than the one for Si-O-Si or Si-O-B. This is probably not a real feature but is likely related to the fact that we have only very few of these angles.)

C. Dielectric constants

The dielectric properties of our eight NBS glass samples have been computed by using the density functional perturbation theory features of the VASP package within the PAW methodology [70]. For this we have first extracted the purely electronic dielectric tensor $(\epsilon_\infty)_{ij}$ (also called relative permittivity). As expected for an amorphous material, we have found that this tensor is basically isotropic and diagonal: The average values of the diagonal elements are $(\epsilon_\infty)_{11} = 2.403$, $(\epsilon_\infty)_{22} = 2.406$, and $(\epsilon_\infty)_{33} = 2.409$, while those of the off-diagonal elements are negligible. Hence, we define an orientationally averaged dielectric constant ϵ_∞ (also called high-frequency dielectric constant) as one-third of the trace of this dielectric tensor. The so-obtained value for ϵ_∞ is 2.406. This is somewhat higher than the value for the case of pure silica obtained by Pasquarello and co-workers, who, using also DFT, found 2.0 and 2.1 [40,69], values that agree well with experimental result equal to 2.1 [71]. Although to our knowledge for NBS glasses with the composition considered here the experimental value of ϵ_∞ has not yet been measured, we can exploit the fact that the high-frequency dielectric constant is related to the refractive index n_∞ of the material, $\epsilon_\infty = n_\infty^2$, which leads for our NBS glass to a value of $n_\infty \approx 1.55$. This value can be compared with the experimental result of 1.52 for the far-infrared refractive index of a NBS glass with a composition quite similar to our glass, i.e., 27.8% $\mathrm{Na_2O}$-11.1% $\mathrm{B_2O_3}$-61.1 $\mathrm{SiO_2}$, corresponding to $R = 2.5$ and $K = 5.5$ [72]. From the good agreement between these two values for n_∞ we can conclude that this quantity probably does not depend strongly on the composition of the glass, in agreement with experimental findings for series of NBSs and aluminosilicate glasses [72,73].

Furthermore, it is also possible to calculate the static dielectric constant ϵ_0, which reflects the ionic displacement contributions to the dielectric constant. For this, one makes use of the Born effective charges introduced above as well as the vibrational modes and eigenfrequencies, the latter ones have been obtained as explained in Sec. IV. ϵ_0 can then be expressed as [69]

$$\epsilon_0 = \epsilon_\infty + \frac{4\pi}{3V}\sum_p\sum_j \frac{\left|\mathcal{F}_j^p\right|^2}{\omega_p}, \tag{9}$$

where the so-called oscillator strength $\mathcal{F}_j^p$ is defined as

$$\mathcal{F}_j^p = \sum_{I,k} Z_{I,jk}\frac{\mathbf{e}_{I,k}(\omega_p)}{\sqrt{m_I}}. \tag{10}$$

Using our value for the high-frequency dielectric constant, $\epsilon_\infty = 2.406$, the above formula gives an average dielectric constant ϵ_0 of 6.62. This result compares well with experimental values for more complex NBS glasses with low sodium content for which ϵ_0 ranges between 5.5 and 6.1 [74]. Furthermore, we mention that for the case of pure silica the DFT calculations predict values between 3.6 and 3.8 [40,69], results that are close to the experimental findings. Hence, we can conclude that, in contrast to the high-frequency dielectric constant for which we have found only a relatively weak dependence on the glass composition, ϵ_0 depends quite strongly on the type of glass considered.

D. Dielectric functions: Infrared spectra

A further observable of interest is the frequency dependence of the dielectric function $\epsilon(\omega)$. This complex quantity can be calculated directly from the eigenmodes and Born effective charges: Writing $\epsilon(\omega) = \epsilon_1(\omega) + i\epsilon_2(\omega)$, the real and imaginary parts are given by [69,75]

$$\epsilon_1(\omega) = \epsilon_\infty - \frac{4\pi}{3V}\sum_p\sum_j \frac{\left|\mathcal{F}_j^p\right|^2}{\omega^2 - \omega_p^2}, \tag{11}$$

$$\epsilon_2(\omega) = \frac{4\pi^2}{3V}\sum_p\sum_j \frac{\left|\mathcal{F}_j^p\right|^2}{2\omega_p^2}\delta(\omega - \omega_n). \tag{12}$$

Closely related to $\epsilon(\omega)$ is the absorption spectra $\alpha(\omega)$, which is given by [72]

$$\alpha(\omega) = 4\pi\omega n''(\omega), \tag{13}$$

with

$$n''(\omega) = \sqrt{\frac{\sqrt{\epsilon_1^2 + \epsilon_2^2} - \epsilon_1}{2}}. \tag{14}$$

This function can be measured directly in experiments and hence will allow us to make a comparison with the prediction from the simulation.

In Fig. 16 we show the imaginary part of the dielectric function $\epsilon_2(\omega)$ and the absorption spectra calculated for our NBS glass samples [panels (a) and (b), respectively]. In panel (a) we have also included the experimental spectra for SiO_2 and B_2O_3 glasses [71,76], and in panel (b) the experimental absorption spectrum obtained for a NBS glass with ratios $R = 2.5$ and $K = 5.5$, i.e., of composition Na_2O-xB_2O_3-$(3-2x)$ SiO_2 with $x = 0.4$ [72]. For the sake of comparison we have scaled the maximum amplitude of each curve to 1.0.

Comparison of the spectra for the three glass-formers shown in Fig. 16(a) makes it possible to identify the origin of the various peaks. First, the spectrum for NBS shows a broad band below 300 cm^{-1}. Since this band is absent in the two other spectra and since we have seen in the VDOS (see Fig. 11) that in this frequency range the vibrational motion is dominated by the Na atoms, we can conclude that the band is related to the sodium atoms.

Furthermore, we notice the presence of a narrow band slightly above 400 cm^{-1}. This feature is also present in the spectrum of pure silica and is known to originate from the bending and rocking motion of oxygen atoms [50,51]. The fact that for NBS the peak is broadened and also shifted somewhat to lower frequencies is probably related to the slight opening of the Si-O-Si bond angles and a softening of the effective Si-O interactions due to the presence of the network modifiers.

The next band is found between 600 and 800 cm^{-1}. In this frequency range the experiments on B_2O_3 and SiO_2 glasses show a peak, the origin of which is attributed to the BO [9,72]. Although we find that in NBS the corresponding band is at somewhat lower frequencies, it can be expected that it has the same origin and that the redshift is due to the presence of the network modifier.

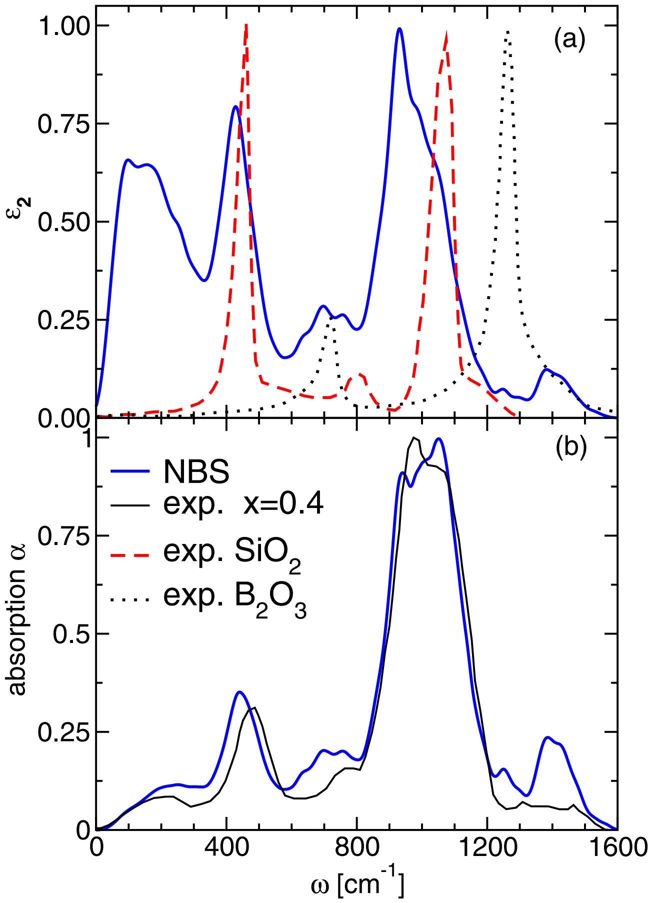

FIG. 16. (Color online) Imaginary part of the dielectric function $\epsilon_2(\omega)$ and absorption spectrum $\alpha(\omega)$, panels (a) and (b), respectively. In panel (a) we have also included the experimental spectra for pure SiO_2 (dashed line) and B_2O_3 (dotted line) glasses [71,76]. For the absorption spectrum $\alpha(\omega)$ (panel b), we also show the experimental spectra for a glass of composition Na_2O-xB_2O_3-$(3-2x)$ SiO_2 for $x = 0.4$ from Ref. [72] (thin solid line). For the sake of comparison we have normalized the maximum amplitude of each spectrum to unity.

At even higher frequencies we can distinguish two bands. The first one ranges from 850 to 1200 cm^{-1}, and it can be assigned to oxygen stretching modes of Si-NBO and Si-BO [77,78]. Earlier analysis of the partial VDOS of a sodium tetrasilicate glass have shown that the main effect of the presence of NBO atoms and the resulting depolymerization of the silica network is the shift of this band to lower frequencies in the NBS spectrum [49]. The second high-frequency band extents between 1200 and 1600 cm^{-1} and, as discussed in the context of Fig. 12, arises from motions of oxygen atoms belonging to borate units, namely the symmetric trigonal ones of $^{[3]}$B. This interpretation is also supported by the fact that the experimental data for B_2O_3, which has mainly $^{[3]}$B units, does have a pronounced peak at these high frequencies as well [included in Fig. 16(b) as well].

Finally, we compare our calculated absorption spectra with the experimental data as measured by Kamitsos *et al.* [72] for the borosilicate described above. From Fig. 16(b) we can conclude that, in general, there is a rather good agreement between the results from the simulations and the experimental data: At low and intermediate frequencies the position and height of the bands are well reproduced. The observed discrepancies can be rationalized by recalling that our samples have a lack of of tetrahedral borate units (see the discussion in the context of Fig. 2), which are expected to contribute to the IR signal in this frequency range [79], in agreement with our findings from Fig. 11, where we showed that in this frequency range the contribution of $^{[4]}$B is much more important than the one of $^{[3]}$B. At higher frequencies there is a very good agreement for the band between 800 and 1200 cm^{-1} inferring that our models reproduce accurately the stretching motions [52] in silicates.

Finally, we see that also the intensity of the band between 1200 and 1600 cm^{-1} is higher than the one of the experiments, but that its position matches the one seen in the real data. Also this discrepancy can likely be traced back to the too-high concentration of $^{[3]}$B units, since (see Fig. 11) they are the only ones that give rise to the density of states in that frequency range.

In this section, we have studied the dielectric properties of our NBS glass samples. The average Born charges of the various species have been computed. For BO and NBO atoms, we have identified the relationships between the values of their Born charges and their bond lengths and bond angles. We have computed the absorption spectrum and we have found it in good agreement with experimental data for a similar composition.

VII. SUMMARY AND CONCLUSIONS

Using *ab initio* MD computer simulations we have investigated the structural, electronic, and vibrational properties of the ternary NBS glass $3Na_2O$-B_2O_3-$6SiO_2$. Particular attention has been given to the coordination of the boron atoms which are found to be present in trigonal and tetrahedral geometries, as expected for this composition. We find that the concentration of these two structural units depends significantly on the fictive temperature of the glass (with $^{[3]}$B decreasing with decreasing T_{fic}), thus affecting the VDOS considerably. However, if one takes into account the measured T dependence of these units, one finds concentrations that are in quantitative agreement with the model proposed by Yun, Dell, and Bray and with estimates from spectroscopic measurements.

Despite the high cooling rate with which the glass sample has been produced, the accuracy of the interactions allows us to study the local structure of the various structural units. In particular, we have investigated how the Na atoms are distributed around the $^{[3]}$B triangles and $^{[4]}$B tetrahedra. From this analysis we can rationalize why the first peak of the radial distribution functions between B and Na is broadened and also understand why the number of Na that share one or two oxygen atoms with the central B atom depends on whether one considers $^{[3]}$B or $^{[4]}$B structures. Furthermore, we see from these Na distributions that the nature of a $^{[4]}$B tetrahedron is different from a SiO_4 tetrahedron in that the former gives rise to a distribution that is significantly more structured.

From the partial VDOS we can conclude that the $^{[3]}$B and $^{[4]}$B units have very different spectral signatures. In particular, we have demonstrated that these spectra make it possible to distinguish clearly whether a $^{[3]}$B unit is symmetric or asymmetric. For the $^{[4]}$B we show that the spectrum can also be used to gain information on the nature of the second-nearest neighbor (i.e., whether it is a B or Si atom). This study reports the first calculation and assignment of the VDOS in a ternary borosilicate glass. Although to our knowledge there are no experimental VDOS data obtained from inelastic neutron diffusion measurements, we expect our results to be in agreement with experiments due to the use of the *ab initio* approach. We mention also that the VDOS extracted from effective force fields simulations presents often a rather poor agreement with experiments and that one of the reasons is that the nature of the vibrational modes is not correctly reproduced by the effective force field approach, as has been shown for the silica glass [80].

We have also calculated the dielectric function $\epsilon(\omega)$ as well as the absorption spectra. The latter is in good quantitative agreement with experimental data, thus showing that the simulation is reliable also for this type of observable. This shows that this type of simulation can be used to predict, e.g., the properties related to the radiative insulation of glasses.

Finally, we have investigated the correlation between the Born effective charge of an oxygen atom and its surrounding geometry. We have found that for the NBO there is a linear correlation of this charge with the distance from the associated Si/B atom. For the BO we find a linear dependence of the charge with the angle spanned by its two bonds. These charge dependencies show that for this type of glasses it is unlikely that a rigid ion model will be able to give a reliable description of the local structure since such models do not take into account the observed charge transfer.

The results described in the present work as well as the ones in the companion paper [10] confirm that the *ab initio* simulations give access to a better understanding of complex borosilicate liquids and glasses since the structural, dynamical, electronic, as well as the vibrational properties can be extracted with a good accuracy and compare very well to experimental data. These simulations can further be used as benchmarks for classical MD simulations as well as to fit more accurate effective potentials [81]. Within the framework of classical simulations, it will then be possible to extensively explore these ternary compositions under varying temperature and pressure conditions using large system size and hence to obtain statistical accuracy that is not accessible in *ab initio* simulations.

ACKNOWLEDGMENTS

We thank D. R. Neuville and B. Hehlen for stimulating discussions on this work. We would also like to thank E. I. Kamitsos for providing experimental data set for IR spectra from Ref. [72]. Financial support from the Agence Nationale de la Recherche (France) under Project POSTRE (ANR-08-MAPR-007) is acknowledged. This work was performed using HPC resources from GENCI French national computer centers (TGCC/CINES/IDRIS) (Grants No. x2010095045, No. x2011095045, No. and x2012095045), and also on the HPC@LR cluster, Montpellier, France. W.K. acknowledges support from the Institut Universitaire de France (France).

[1] A. Varshneya, *Fundamentals of Inorganic Glasses*, 2nd ed. (Society of Glass Technology, Sheffield, U.K., 2006).

[2] Y. Yun and P. Bray, J. Non-Cryst. Solids **27**, 363 (1978).

[3] Y. Yun, S. Feller, and P. Bray, J. Non-Cryst. Solids **33**, 273 (1979).

[4] W. Dell, P. Bray, and S. Xiao, J. Non-Cryst. Solids **58**, 1 (1983).

[5] B. G. Parkinson, D. Holland, M. E. Smith, A. P. Howes, and C. R. Scales, J. Non-Cryst. Solids **353**, 4076 (2007).

[6] B. G. Parkinson, D. Holland, M. E. Smith, A. P. Howes, and C. R. Scales, J. Phys. Condens. Matter **19**, 415114 (2007).

[7] B. G. Parkinson, D. Holland, M. E. Smith, C. Larson, J. Doerr, M. Affatigato, S. A. Feller, A. P. Howes, and C. R. Scales, J. Non-Cryst. Solids **354**, 1936 (2008).

[8] D. Manara, A. Grandjean, and D. R. Neuville, J. Non-Cryst. Solids **355**, 2528 (2009).

[9] D. Manara, A. Grandjean, and D. R. Neuville, Am. Mineral. **94**, 777 (2009).

[10] L. Pedesseau, S. Ispas, and W. Kob, Phys. Rev. B **91**, 134201 (2015).

[11] G. Kresse and J. Furthmüller, Phys. Rev. B **54**, 11169 (1996).

[12] G. Kresse and J. Furthmüller, Comput. Mat. Sci. **6**, 15 (1996).

[13] O. V. Mazurin, T. P. Shvaiko-Shvaikovskaya, and M. Streltsina, *Handbook of Glass Data: Ternary Silicate Glasses, Part C* (Elsevier Science, Amsterdam, 1984).

[14] W. Kohn and L. J. Sham, Phys. Rev. **140**, A1133 (1965).

[15] R. Martin, *Electronic Stucture: Basic Theory and Practical Methods* (Cambridge University Press, Cambridge, 2004).

[16] J. P. Perdew, K. Burke, and M. Ernzerhof, Phys. Rev. Lett. **77**, 3865 (1996).

[17] J. P. Perdew, A. Ruzsinszky, G. I. Csonka, O. A. Vydrov, G. E. Scuseria, L. A. Constantin, X. Zhou, and K. Burke, Phys. Rev. Lett. **100**, 136406 (2008).

[18] P. E. Blöchl, Phys. Rev. B **50**, 17953 (1994).

[19] S. Ispas, M. Benoit, P. Jund, and R. Jullien, Phys. Rev. B **64**, 214206 (2001).

[20] D. Donadio, M. Bernasconi, and F. Tassone, Phys. Rev. B **70**, 214205 (2004).

[21] J. Du and L. R. Corrales, J. Chem. Phys. **125**, 114702 (2006).

[22] S. Ispas, T. Charpentier, F. Mauri, and D. R. Neuville, Solid State Sci. **12**, 183 (2010).

[23] A. Tilocca, J. Chem. Phys. **129**, 084504 (2008).

[24] H. Inoue, A. Masuno, and Y. Watanabe, J. Phys. Chem. B **116**, 12325 (2012).

[25] K. Vollmayr, W. Kob, and K. Binder, Phys. Rev. B **54**, 15808 (1996).

[26] S. Sen, Z. Xu, and J. F. Stebbins, J. Non-Cryst. Solids **226**, 29 (1998).

[27] S. Sen, J. Non-Cryst. Solids **253**, 84 (1999).

[28] T. J. Kiczenski, L.-S. Du, and J. F. Stebbins, J. Non-Cryst. Solids **351**, 3571 (2005).

[29] F. Angeli, O. Villain, S. Schuller, T. Charpentier, D. de Ligny, L. Bressel, and L. Wondraczek, Phys. Rev. B **85**, 054110 (2012).

[30] O. Majerus, L. Cormier, G. Calas, and B. Beuneu, Phys. Rev. B **67**, 024210 (2003).

[31] J. Wu, M. Potuzak, and J. F. Stebbins, J. Non-Cryst. Solids **357**, 3944 (2011).

[32] S. Sen, T. Topping, P. Yu, and R. E. Youngman, Phys. Rev. B **75**, 094203 (2007).

[33] M. Fleet and S. Muthupari, J. Non-Cryst. Solids **255**, 233 (1999).

[34] J. Swenson, L. Börjesson, and W. S. Howells, Phys. Rev. B **52**, 9310 (1995).

[35] L.-H. Kieu, J.-M. Delaye, L. Cormier, and C. Stolz, J. Non-Cryst. Solids **357**, 3313 (2011).

[36] M. Fábián, E. Sváb, G. Mészáros, Z. Révay, T. Proffen, and E. Veress, J. Non-Cryst. Solids **353**, 2084 (2007).

[37] S. Wang and J. F. Stebbins, J. Am. Ceram. Soc. **82**, 1519 (1999).

[38] J. F. Stebbins and S. Sen, J. Non-Cryst. Solids **224**, 80 (1998).

[39] A. Takada, C. Catlow, and G. Price, J. Phys. Condens. Matter **7**, 8693 (1995).

[40] L. Giacomazzi, P. Umari, and A. Pasquarello, Phys. Rev. B **79**, 064202 (2009).

[41] M. Benoit, S. Ispas, and M. E. Tuckerman, Phys. Rev. B **64**, 224205 (2001).

[42] A. Tilocca, J. Chem. Phys. **133**, 014701 (2010).

[43] F. Michel, L. Cormier, P. Lombard, B. Beuneu, L. Galoisy, and G. Calas, J. Non-Cryst. Solids **379**, 169 (2013).

[44] S. Ohmura and F. Shimojo, Phys. Rev. B **78**, 224206 (2008).

[45] L.-S. Du and J. F. Stebbins, J. Phys. Chem. B **107**, 10063 (2003).

[46] L.-S. Du, J. Allwardt, B. Schmidt, and J. Stebbins, J. Non-Cryst. Solids **337**, 196 (2004).

[47] P. Umari and A. Pasquarello, Phys. Rev. Lett. **95**, 137401 (2005).

[48] G. Ferlat, T. Charpentier, A. P. Seitsonen, A. Takada, M. Lazzeri, L. Cormier, G. Calas, and F. Mauri, Phys. Rev. Lett. **101**, 065504 (2008).

[49] S. Ispas, N. Zotov, S. De Wispelaere, and W. Kob, J. Non-Cryst. Solids **351**, 1144 (2005).

[50] S. N. Taraskin and S. R. Elliott, Phys. Rev. B **56**, 8605 (1997).

[51] A. Pasquarello, J. Sarnthein, and R. Car, Phys. Rev. B **57**, 14133 (1998).

[52] D. D. S. Meneses, M. Eckes, L. del Campo, C. N. Santos, Y. Vaills, and P. Echegut, Vib. Spectrosc. **65**, 50 (2013).

[53] T. Yano, N. Kunimine, S. Shibata, and M. Yamane, J. Non-Cryst. Solids **321**, 137 (2003).

[54] G. Simon, B. Hehlen, R. Vacher, and E. Courtens, J. Phys. Condens. Matter **20**, 155103 (2008).

[55] C. P. Varsamis, E. I. Kamitsos, and G. D. Chryssikos, Phys. Rev. B **60**, 3885 (1999).

[56] U. Buchenau, N. Nücker, and A. J. Dianoux, Phys. Rev. Lett. **53**, 2316 (1984).

[57] E. Courtens, M. Foret, B. Hehlen, B. Rufflé, and R. Vacher, J. Phys. Condens. Matter **15**, S1279 (2003).

[58] J. Horbach, W. Kob, and K. Binder, J. Phys. Chem. B **103**, 4104 (1999).

[59] J. Sarnthein, A. Pasquarello, and R. Car, Phys. Rev. B **52**, 12690 (1995).

[60] M. Benoit, S. Ispas, P. Jund, and R. Jullien, Eur. Phys. J. B **13**, 631 (2000).

[61] K. Burke, J. Chem. Phys. **136**, 150901 (2012).

[62] J. Du and L. R. Corrales, J. Phys. Chem. **110**, 22346 (2006).

[63] R. F. W. Bader, *Atoms in Molecule: A Quantum Theory* (Oxford University Press, Oxford, U.K., 1990).

[64] G. Henkelman, A. Arnaldsson, and H. Jónsson, Comput. Mater. Sci. **36**, 354 (2006).

[65] R. Brückner, H.-U. Chun, H. Goretzki, and M. Sammet, J. Non-Cryst. Solids **42**, 49 (1980).

[66] T. Uchino, M. Iwasaki, T. Sakka, and Y. Ogata, J. Phys. Chem. **95**, 5455 (1991).

[67] M. A. Zwijnenburg, C. van Alsenoy, and T. Maschmeyer, J. Phys. Chem. A **106**, 12376 (2002).

[68] X. Gonze and C. Lee, Phys. Rev. B **55**, 10355 (1997).

[69] A. Pasquarello and R. Car, Phys. Rev. Lett. **79**, 1766 (1997).

[70] M. Gajdoš, K. Hummer, G. Kresse, J. Furthmüller, and F. Bechstedt, Phys. Rev. B **73**, 045112 (2006).

[71] H. Philipp, in *Handbook of Optical Constants of Solids*, edited by D. Palik (Academic Press, San Diego, 1998), pp. 749–763.

[72] E. I. Kamitsos, J. A. Kapoutsis, H. Jain, and C. H. Hsieh, J. Non-Cryst. Solids **171**, 31 (1994).

[73] C. H. Hsieh, H. Jain, and E. I. Kamitsos, J. Appl. Phys. **80**, 1704 (1996).

[74] Z. Wang, Y. Hu, H. Lu, and F. Yu, J. Non-Cryst. Solids **354**, 1128 (2008).

[75] M. F. Thorpe and S. W. de Leeuw, Phys. Rev. B **33**, 8490 (1986).

[76] F. L. Galeener, G. Lucovsky, and J. C. Mikkelsen, Phys. Rev. B **22**, 3983 (1980).

[77] F. Domine and B. Piriou, J. Non-Cryst. Solids **55**, 125 (1983).

[78] C. I. Merzbacher and W. B. White, Am. Mineral. **73**, 1089 (1988).

[79] E. I. Kamitsos, Y. D. Yiannopoulos, C. P. Varsamis, and H. Jain, J. Non-Cryst. Solids **222**, 59 (1997).

[80] M. Benoit and W. Kob, Europhys. Lett. **60**, 269 (2002).

[81] A. Carré, J. Horbach, S. Ispas, and W. Kob, Europhys. Lett. **82**, 17001 (2008).